The three-dimensional structure of momentum transfer in turbulent channels

Adrián Lozano-Durán[1]†, Oscar Flores[2] and Javier Jiménez[1,3]

[1] School of Aeronautics, Universidad Politécnica de Madrid, 28040 Madrid, Spain

[2] Department Mechanical Engineering, University of Washington Seattle, WA 98195, USA

[3] Centre for Turbulence Research, Stanford University, Stanford, CA 94305, USA

The quadrant analysis of the intense tangential Reynolds stress in plane turbulent channels is generalized to three-dimensional structures (Qs), with special emphasis on the logarithmic and outer layers. Wall-detached Qs are background stress fluctuations. They are small and isotropically oriented, and their contributions to the mean stress cancel. Wall-attached Qs are larger, and carry most of the mean Reynolds stresses. They form a family of roughly self-similar objects that become increasingly complex away from the wall, resembling the vortex clusters in del Álamo *et al.* (*J. Fluid Mech.*, vol. 561, 2006, pp. 329–358). Individual Qs have fractal dimensions of the order of $D = 2$, slightly fuller than the clusters. They can be described as 'sponges of flakes', while vortex clusters are 'sponges of strings'. The number of attached Qs decays away from the wall, but the fraction of the stress that they carry is independent of their sizes. A substantial fraction of the stress resides in a few large objects extending beyond the centreline, reminiscent of the very large structures of several authors. The predominant logarithmic-layer structure is a side-by-side pair of a sweep (Q4) and an ejection (Q2), with an associated cluster, and shares dimensions and stresses with the conjectured attached eddies of Townsend (*J. Fluid Mech.*, vol. 11, 1961, pp. 97–120). Those attached eddies tend to be aligned streamwise from each other, located near the side walls between the low- and high-velocity large-scale streaks, but that organization does not extend far enough to explain the very long structures in the centre of the channel.

Key words: turbulence simulation, turbulent flows, turbulent boundary layers

---

1. Introduction

One of the most ubiquitous properties of turbulent flows is the enhancement of transport processes, such as mass, heat or momentum, and the success of many engineering devices depends of our ability to control and predict those processes. Of particular interest is the transport of momentum, which is responsible for the increased drag of wall-bounded turbulent flows, and for their characteristically flattened mean-velocity profiles. The object of the present work is to study the structure of the intense Reynolds stresses that carry most of the wall-normal flux of momentum, particularly in the logarithmic and outer layers.

† Email address for correspondence: adrian@torroja.dmt.upm.es

The study of the statistical properties of the Reynolds stresses began in the late 1960s, with the observation by Kline *et al.* (1967) that the near-wall low-velocity streaks undergo a process of lift-up, oscillation, break-up and ejection, which they called bursting. Kim, Kline & Reynolds (1971) showed that most of the turbulence production in the near-wall region occurs during those bursts, and several conditional-sampling techniques were developed to identify the structures involved in the process. Examples are the *u*-level detection of Lu & Willmarth (1973), the VITA (variable-interval time average) of Blackwelder & Kaplan (1976) and the VISA (variable-interval space average) of Kim (1985). Several of those techniques were surveyed by Bogard & Tiederman (1986), who concluded that the best compromise between detection probability and false positives was provided by the quadrant analysis of Wallace, Eckelman & Brodkey (1972), Willmarth & Lu (1972) and Lu & Willmarth (1973), in which points of the flow are classified in terms of the quadrant of the parameter plane of streamwise and wall-normal velocity fluctuations. Q1 events (outward interactions) have $u > 0$ and $v > 0$, Q2 events (ejections) have $u < 0$ and $v > 0$, Q3 events (inward interactions) have $u < 0$ and $v < 0$ and Q4 events (sweeps) have $u > 0$ and $v < 0$. Hereafter, Q events will be referred to simply as Qs, and we will occasionally group the 'gradient' Q2s and Q4s as Q^-, and the 'counter-gradient' Q1s and Q3s as Q^+.

Throughout the paper, u, v and w are streamwise, wall-normal and spanwise velocities, and are usually understood to refer to fluctuations with respect to the mean. The streamwise and spanwise coordinates are, respectively, x and z. The wall-normal coordinate, y, is zero at the wall. Overlined ($\overline{\varphi}$) and primed (φ') variables respectively denote averaged values and root-mean-squared (r.m.s.) intensities of the fluctuations, computed over the homogeneous directions and time. The channel half-width or boundary-layer thickness is h, and the '+' superscript denotes wall units defined in terms of the friction velocity u_τ and of the kinematic viscosity ν. We often classify results as relating to the buffer, logarithmic or outer regions, arbitrarily defined as $y^+ < 100$, $100\nu/u_\tau < y < 0.2h$ and $y > 0.2h$, respectively. Varying the limits of the logarithmic layer within the usual range did not significantly alter the results.

Although most of the early work focused on bursting in the buffer region, studies during the 1990s began to establish a relationship between near-wall bursting and outer structures. Antonia, Bisset & Browne (1990) applied a variant of the *u*-level method (WAG, window average gradient) to boundary layers with relatively high Reynolds numbers based on the momentum thickness, $Re_\theta = U_\infty\theta/\nu = 1360$–$9630$, corresponding to $h^+ = 530$–3100. They reported that outer-scale discontinuities in the streamwise velocity, extending across the whole thickness of the boundary layer, tend to be located near the upstream end of the near-wall bursts. Wark & Nagib (1991) applied quadrant analysis to a boundary layer at $Re_\theta = 4650$ ($h^+ = 1500$), and found large conditional events with sizes of the order of h. Using a related identification technique in the atmospheric boundary layer, Narasimha *et al.* (2007) described Reynolds-stress structures with lengths comparable to the distance to the wall that, because of the high Reynolds number involved, were both very long in wall units and very short compared with the boundary layer thickness. Hoyas & Jiménez (2006) showed that the spectral signatures of the very-large motions (Jiménez 1998; Kim & Adrian 1999), or global modes (del Álamo *et al.* 2004), characteristic of the outer region are present at the wall, as well as those of similar smaller structures in the logarithmic layer, and Hutchins & Marusic (2007*b*) showed that part of that influence is a modulation of the intensity of the small-scale buffer-layer fluctuations.

More recently, Flores & Jiménez (2010*a*) showed that the hierarchy of structures of increasing sizes postulated by Townsend (1961) for the logarithmic layer can be represented numerically in computational boxes of widths proportional to the height to be studied. Each box contains a single complex structure, including a segment of a streamwise velocity streak and a cluster of vortices, that bursts quasiperiodically to fill the box with essentially normal turbulence, with a strong Q2 and Q4 occurring simultaneously. The existence of a hierarchy of Q2s and Q4s was also conjectured by Wark & Nagib (1991), and is consistent with the similarity observed by Kailas & Narasimha (1994) between the conditionally sampled structures extracted from the near-wall region of laboratory boundary layers and those in the logarithmic region of the atmospheric boundary layer.

Q2s and Q4s play important roles in most of the structural models proposed to explain how turbulent kinetic energy and momentum are redistributed in wall-bounded turbulence. The majority of these models (see the review by Robinson 1991) are loosely based on the attached-eddy hypothesis of Townsend (1961) and involve wall-attached vortical loops growing from the wall into the outer region (Perry, Henbest & Chong 1986). More recently, in order to account for the very large-scale motions mentioned above, as well as for earlier experimental evidence on the internal structure of the bursts (Bogard & Tiederman 1986), a variant model has evolved to include vortex packets (Adrian, Meinhart & Tomkins 2000), in which trains of hairpin vortices grow from the wall by a process of merging (Tomkins & Adrian 2003) and self-regeneration (Zhou *et al.* 1999). The heads of the hairpins are arranged into inclined shear layers generated by the combined induction of the hairpins of the packet, with a Q4 upstream and above the packet and a Q2 beneath it. Ganapathisubramani, Longmire & Marusic (2003) used PIV data on wall-parallel planes in a boundary layer with $Re_\theta = 2500$ ($h^+ = 1060$) to quantify the contribution to the Reynolds stresses by packets of hairpins. They report that, at $y^+ = 100$, packets covering 4 % of the area produce 28 % of the total Reynolds stresses.

The hairpin-packet model is usually understood to involve relatively smooth vortex loops as the structures associated with Townsend's (1976) attached eddies, although recent discussions tend to include 'canes, heads, legs and three-quarter hairpin shapes, generally asymmetric and distorted' into the class of 'hairpin-like' vortices (Dennis & Nickels 2011*a*), making them hard to distinguish from generic vortices. An alternative, less organized, structure was proposed by del Álamo *et al.* (2006), who analysed the statistical properties of clusters of vortices (clusters hereafter) in direct numerical simulations (DNSs) of turbulent channels with $h^+ = 550–1880$. The clusters segregate into wall-attached and wall-detached families. The wall-detached clusters are dissipative objects, with sizes that scale with the local Kolmogorov scale. The attached ones form a self-similar family of objects that mark strong Q2s. The averaged flow conditioned to an attached cluster consist on an elongated low-velocity streak extending downstream of the cluster, flanked by a pair of shorter high-velocity streaks. While this averaged structure is consistent with the hairpin packet paradigm, del Álamo *et al.* (2006) pointed out that the instantaneous clusters are more complex, in agreement with earlier visualizations by Tanahashi *et al.* (2004).

The models based on hairpin packets and on attached clusters are roughly equivalent kinematically, but they are dynamically different. While the hairpin packets grow from the buffer region, there is evidence suggesting that the wall-normal velocity structures marked by the clusters do not. Not only are the statistics of the clusters not affected when the buffer region is completely destroyed by an artificial forcing (Flores, Jiménez & del Álamo 2007), but their lifetimes are too short to account for their sizes (del

Álamo *et al.* 2006). The linear model of Flores & Jiménez (2010*b*) predicts that the disturbances of the wall-normal velocity grow little before being dissipated by the background turbulence, and suggests that the ejections marked by the clusters must be created at (or close to) their observed heights.

In this paper we study the statistical properties of the coherent structures responsible for the Reynolds stresses and the momentum transfer, and their possible relationship with vortex clusters. We generalize to three dimensions the quadrant analysis of Wallace *et al.* (1972) and Lu & Willmarth (1973), in a manner analogous to the method used by del Álamo *et al.* (2006) to study clusters. To our knowledge, this is the first time that a full, three-dimensional, characterization of the Qs has been presented.

The question of the interest of the structural studies to which this paper belongs was raised by one of the referees and deserves some comment. It is clear that the most interesting results are not the kinematic description of the structures in individual flow realizations, but the elucidation of how they relate to each other, and how and why they evolve in time. For example, how the energy or the momentum are exchanged among different structures and flow scales. Such dynamical studies have been difficult in the past, because it has been hard to obtain time-resolved information of three-dimensional structures, but that limitation is beginning to be relaxed. The early studies by Robinson (1991) of animations of the simulation of a boundary layer by Spalart (1988), and the minimal-box simulations by Jiménez & Moin (1991) and others, continued older experimental work using tracers in the buffer layer. More recently, it has become possible to extend time-dependent analysis to the logarithmic layer. Examples are the previously cited small-box simulations by Flores & Jiménez (2010*a*), the analysis of the temporal evolution of vortex clusters in Lozano-Durán & Jiménez (2010) or the recent analysis of vortex packets in a boundary layer by Lee & Sung (2011). However, in a continuous system such as a fluid, any such study depends on the choice of which structures to track. Most analyses of the buffer-layer, which is essentially a one-scale system, centred on vorticity, which is easily identifiable and representative of other quantities in that region. The initial extensions to the logarithmic layer followed the same method, although that region is multiscale and different quantities are associated with different scales. For example, it soon became clear that neither the vortex clusters in del Álamo *et al.* (2006) nor the hairpin packets in Adrian (2007) are single-scale objects. The present paper deals with the characterization of a different candidate for time-dependent analysis, including its relation with previously studied structures. As argued above, Qs are important for the transfer of momentum and for the generation of turbulent energy, and can be considered as lying at the top of the turbulent cascade. They have also been studied enough in the past, typically as one-dimensional sections, to provide some continuity of the present paper with earlier work. The further study of their temporal evolution, especially in relation to other flow structures, would require different data and techniques and cannot be tackled at present, but should become easier in the near future.

The paper is organized as follows. Section 2 describes the numerical database and the method employed to identify Qs, which are classified in § 3. The statistical properties of the attached Q2s and Q4s are presented in §§ 4 and 5, and their relative positions and organization are described in § 6. Finally, the results are discussed in § 7 and conclusions are offered. A preliminary report on the present results is Flores & Jiménez (2008).

Case	h^+	L_x/h	L_z/h	Δx^+	Δz^+	N_y	N_F	N_Q	N_V
L950	934	8π	3π	11	5.7	385	21	4.6×10^5	9.6×10^5
L2000	2003	8π	3π	12	6.1	633	8	8.3×10^5	2.1×10^6

TABLE 1. Parameters of the simulations. Here L_x and L_z are the streamwise and spanwise dimensions of the numerical box and h is the channel half-width; Δx and Δz are the resolutions in terms of Fourier modes before dealiasing; N_y is the number of wall-normal collocation points; N_F is the number of fields used to accumulate statistics and N_Q and N_V are the numbers of Q⁻s and of clusters extracted for the reference values of the identification thresholds.

2. Numerical experiments and identification method

We use data from the DNSs of turbulent channels by del Álamo *et al.* (2004) at $h^+ = 934$ (case L950) and by Hoyas & Jiménez (2006) at $h^+ = 2003$ (case L2000). Their parameters are summarized in table 1. The incompressible flow is integrated in the form of evolution equations for the wall-normal vorticity and for the Laplacian of the wall-normal velocity, as in Kim, Moin & Moser (1987), and the spatial discretization is dealiased Fourier in the two wall-parallel directions. Case L950 uses Chebychev polynomials in y and L2000 uses seven-point compact finite differences. Time stepping is the third-order semi-implicit Runge–Kutta in Moser, Kim & Mansour (1999). Both channels have large computational domains in the streamwise and spanwise directions, to ensure that the largest structures of the flow are reasonably well represented. Note that the Reynolds numbers of the simulations are comparable to those of most of the laboratory experiments mentioned in the introduction.

To investigate the statistical properties of the intense structures contributing most to the Reynolds stresses, we extend the one-dimensional quadrant analysis of Lu & Willmarth (1973) to three dimensions. We define the Qs as connected regions satisfying

$$|\tau(\mathbf{x})| > Hu'(y)v'(y), \tag{2.1}$$

where $\tau(\mathbf{x}) = -u(\mathbf{x})v(\mathbf{x})$ is the instantaneous point-wise tangential Reynolds stress and the hyperbolic-hole size H is discussed below. Connectivity is defined in terms of the six orthogonal neighbours in the Cartesian mesh of the DNS, and an object is classified as belonging to the different quadrants according to the signs of the mean u_m and v_m, computed over the domain Ω of all of its constituent points,

$$v_m = \frac{\displaystyle\int_\Omega v \, dV}{\displaystyle\int_\Omega dV}, \tag{2.2}$$

with a similar definition for u_m. It will be shown in figure 4(*a*) that this classification is essentially unambiguous. To identify correctly the Qs of the upper channel half, we change the sign of their v_m. That allows connected Q2s and Q4s to extend beyond the central plane, even if, otherwise, they would be classified as Q3s and Q1s over part of their volumes. On the other hand, it leads to distortions in the statistics of the quadrant contributions near the centre of the channel ($y/h \gtrsim 0.7$), because some of the stresses are included with the wrong sign (see figure 2*b*, discussed in § 3).
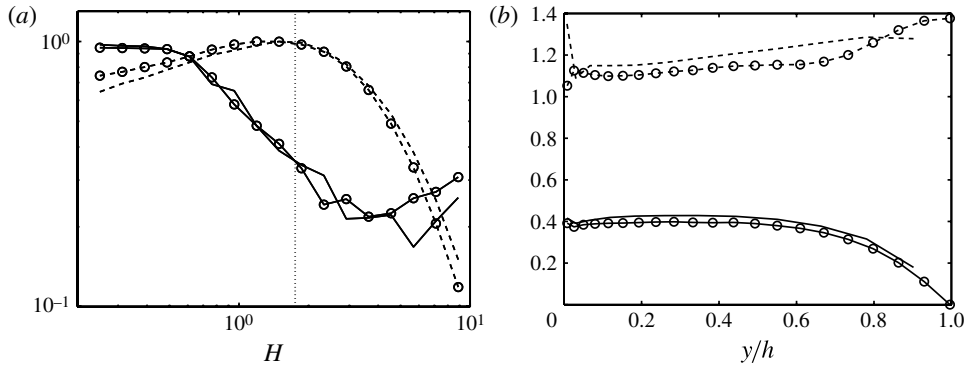
FIGURE 1. (*a*) Percolation diagram for the identification of Qs. ——, Ratio of the volume of the largest object to the volume of all identified objects, V_{lar}/V_{tot}; – – –, ratio of the number of identified objects to the maximum number of objects, N/N_{max}. The vertical dotted line indicates the chosen threshold, $H = 1.75$. (*b*) Profiles of the ratios $\bar{\tau}/\overline{(u'v')}$ (——) and $\tau'/\overline{(u'v')}$ (– – –). In both panels, lines without symbols correspond to L950, and those with symbols correspond to L2000.

Note that the threshold in (2.1) depends on the wall distance. As noted by Nagasoa & Handler (2003), using an identification method with a constant threshold, such as $|\tau| > Hu'(y_0)v'(y_0)$, with some reference y_0, is problematic in inhomogeneous flows. In our case, very few objects are recovered in the outer region if y_0 is chosen in the buffer layer, while choosing a high y_0 results in a confusingly cluttered buffer layer. This behaviour agrees with the observations of Blackburn, Mansour & Cantwell (1996) and worsens as *Re* increases. Our choice of the local standard deviation in (2.1) results in a roughly constant contribution of the Qs to the Reynolds stress and agrees with a similar choice in del Álamo *et al.* (2006) for the identification of vortex clusters.

As argued by Bogard & Tiederman (1986), quadrant analysis depends on the value of the hyperbolic-hole size H. They report that the optimum threshold for the buffer region is $H \approx 1$, based on direct comparisons between the detected events and instantaneous visualizations of the flow. We choose H based on the percolation behaviour of (2.1). Percolation theory describes the statistics of the connected components of a random graph. Here, it is applied to the variation with H of the volume of the connected objects extracted by (2.1), as first used to identify vorticity and dissipation structures in isotropic turbulence by Moisy & Jiménez (2004) and in channels by del Álamo *et al.* (2006).

Figure 1(*a*) shows the percolation diagram of (2.1) in the two channels considered here. The solid lines are the ratio of the volume of the largest identified object, V_{lar}, to the total volume V_{tot} satisfying (2.1), and the dashed ones are the total number of identified objects, N/N_{max}, normalized with its maximum over H. When $H \gtrsim 3$, the identification only yields a few small objects that correspond to the strongest Qs. Decreasing H introduces new Qs, while previously identified ones grow in size. At first, the size of the largest Q changes little, and V_{lar}/V_{tot} stays roughly constant, but eventually the objects start to merge, resulting in a rapid increase of V_{lar}/V_{tot} and in a decrease of the number of objects. Figure 1(*a*) shows that this percolation crisis takes place in the range $0.5 \lesssim H \lesssim 3$, independently of the Reynolds number. For lower thresholds, $V_{lar}/V_{tot} \approx 1$, and most of the volume satisfying (2.1) belongs to a single object.
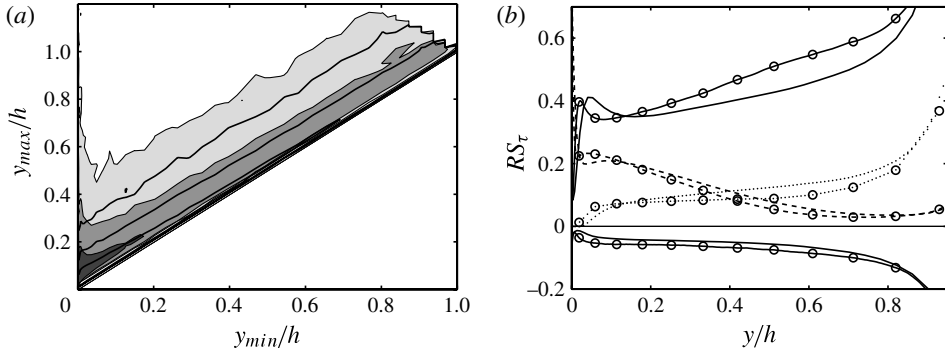
FIGURE 2. (*a*) Probability density function of the maximum and minimum wall distances of the identified Q$^-$s, $p(y_{min}, y_{max})$. The contours are 0.1, 1 and 10, from lighter to darker. Shaded contours are L950 and lines are L2000. (*b*) RS_τ, fraction of the total Reynolds stresses from: —— (positive), attached Q2; – – –, attached Q4; . . . . . ., detached Q$^-$; —— (negative), all Q$^+$. Lines without symbols for L950, lines with symbols for L2000.

The vertical dashed line in figure 1(*a*) shows the threshold used in the present work, $H = 1.75$, chosen to maximize the number of objects. Some of the effects of changing H are discussed in later sections to illustrate specific points, but, in general, the results are qualitatively similar within the range $1 \lesssim H \lesssim 3$.

To avoid the high cost of evaluating (2.1) in the full domain for $H \lesssim 0.5$, we followed del Álamo *et al.* (2006) and all data points in figure 1 were generated by applying (2.1) to sub-boxes of size $6h \times h \times 3h$ in the three Cartesian directions, rather than to the full computational domain ($25h \times 2h \times 12h$). The low values of V_{lar}/V_{tot} at the chosen threshold (figure 1*a*), and the agreement between both Reynolds numbers, give some confidence that the percolation diagram is not strongly influenced by that simplification. The rest of the data in the paper are obtained applying (2.1) to full flow fields.

The threshold selected, $H = 1.75$, compares well with the one recommended by Bogard & Tiederman (1986) for bursts in the buffer region, but some care is needed when comparing it with other published values. The Reynolds stresses in (2.1) are normalized with the r.m.s. of the velocity fluctuations u' and v', as in Lu & Willmarth (1973) and Bogard & Tiederman (1986), but other normalizations are also found in the literature. The original analysis in Willmarth & Lu (1972) used multiples of the local mean Reynolds stress,

$$|\tau(\boldsymbol{x})| > \widetilde{H}|\overline{\tau}|(y), \tag{2.3}$$

while the more recent paper by Narasimha *et al.* (2007) proposes the r.m.s. of the stress fluctuations,

$$|\tau(\boldsymbol{x})| > \widehat{H}\tau'(y), \tag{2.4}$$

together with a more complicated identification algorithm involving the zero crossings of the instantaneous τ.

Figure 1(*b*) shows that $H, \widetilde{H}$ and $\widehat{H}$ satisfy approximately $\overline{\tau}/(u'v') \approx 0.4$ and $\tau'/(u'v') \approx 1.1$, at least in $y \lesssim 0.7h$, yielding

$$H \approx 0.4\widetilde{H} \approx 1.1\widehat{H}. \tag{2.5}$$

We use those approximations in §3 to compare our results with others in the literature.

As mentioned in the introduction, del Álamo *et al.* (2006) found that wall-attached clusters of vortices are markers for strong Q2s. Hence, we also apply their methodology to extract clusters from the same fields used to extract the Qs. Briefly, a cluster of vortices is a connected region satisfying

$$D(\mathbf{x}) > \alpha D'(y), \tag{2.6}$$

where D is the discriminant of the velocity gradient tensor, $D'(y)$ is its standard deviation and $\alpha = 0.02$ is a thresholding parameter. Connectivity is defined as for the Qs and α is obtained from a similar percolation analysis. Full details can be found in del Álamo *et al.* (2006).

Finally, even if the flow is not isotropic, it will be useful in §3 to define isotropic Reynolds numbers and scales to compare the largest with the smallest Qs. We define the Taylor microscale from $\lambda^2 = 10\nu K/\epsilon$ and the microscale Reynolds number as

$$Re_\lambda = q\lambda/\nu = K(20/3\nu\epsilon)^{1/2}, \tag{2.7}$$

where ϵ is the kinetic energy dissipation rate and K is the turbulent kinetic energy. The large-scale velocity q is defined from $K = 3q^2/2$ as an 'isotropic' fluctuation intensity (Batchelor 1953). The three velocity components are available for the two simulations, and K and ϵ can be computed directly, but we will use in the next section experimental data for which only u and v are known. In those cases, ϵ is computed from the temporal gradients of u, assuming isotropy of the small scales, and converting times to lengths using Taylor's frozen-turbulence hypothesis with the local mean velocity and the kinetic energy is defined as $K = (u'^2 + 2v'^2)/2$. The error of the latter approximation can be estimated from the simulation data to be ∼5 % in the logarithmic layer. The Kolmogorov length is $\eta = (\nu^3/\epsilon)^{1/4}$ and the integral scale is defined as $L_\epsilon = q^3/\epsilon$.

In the logarithmic layer of channels, ϵ can be approximated by the local turbulent energy production, $\epsilon \approx u_\tau^2 \partial_y \bar{u} \approx u_\tau^3/\kappa y$, where $\kappa \approx 0.4$ is the Kármán constant, from where it follows that $\eta^+ \approx (\kappa y^+)^{1/4}$, and that $Re_\lambda \propto \lambda^+ \propto y^{+1/2}$. In practice, the maximum Re_λ of channels is attained at $y \approx 0.4h$, above where it decreases slightly. Table 3 includes typical values for the two simulations and for some experiments at higher Reynolds numbers.

3. Wall-attached and detached objects

The above procedure yields about 10^6 Q⁻s and clusters for each of the two Reynolds numbers under study (see table 1). Objects with volumes smaller than 30^3 wall units are discarded to avoid grid resolution issues and are not included in the table. Although they account for ∼70 % of the number of originally identified Qs, they contain less than 1 % of their volume. For clusters, the small discarded objects are almost 90 % of the total number and contain 1.5 % of the volume. Each object is circumscribed within a box aligned to the Cartesian axes, whose streamwise and spanwise sizes are denoted by Δ_x and Δ_z. The minimum and maximum distances of each object to the closest wall are y_{min} and y_{max}, and $\Delta_y = y_{max} - y_{min}$.

Figure 2(*a*) shows the probability density function (p.d.f.) of the minimum and maximum wall distances for the Q⁻s, and shows that they separate into two families. The first one is formed by the narrow vertical band with $y_{min}^+ < 20$, and corresponds to wall-attached objects. The second family is formed by wall-detached objects with

Case	N_1	N_2	N_3	N_4	V_1	V_2	V_3	V_4
L950 (all)	0.18	0.33	0.19	0.31	0.004	0.056	0.006	0.025
L950 (attached)	0.02	0.15	0.006	0.13	0.000	0.047	0.000	0.015
L2000 (all)	0.19	0.33	0.21	0.28	0.004	0.059	0.008	0.022
L2000 (attached)	0.02	0.14	0.007	0.11	0.000	0.053	0.000	0.014

TABLE 2. The numerical fraction with respect of the total number of objects, N_k, and the volume fraction with respect to the total channel volume, V_k, for the four different types of Qs.

Case	y^+	Re_λ	$\overline{\tau}/u'v'$	$\tau'/u'v'$	L_ϵ/η	λ/η	ℓ/η	L_Q/L_{tot}
L950 (detached)	370	80	0.42	1.15	93	16	20	0.02
L2000 (detached)	800	127	0.39	1.11	187	22	21	0.01
L2000 (all)	800	127	0.39	1.11	187	22	31	0.10
Round jet		415	0.09	0.965	1.1×10^3	40	50	0.05
Plane jet (PJ1)		632	−0.12	0.963	2.1×10^3	49	50	0.03
Plane jet (PJ2)		1090	−0.04	0.962	4.7×10^3	65	76	0.04
ASL	4×10^4	1910	0.34	1.02	1.1×10^4	85	188	0.08

TABLE 3. Characteristic of the Reynolds-stress fluctuations in the channels, and in several high-Reynolds number flows from Antonia & Pearson (1999). The mean length, ℓ, of the Q^-s is defined for $H = 1.75$, estimated using Taylor's advection hypothesis with the local mean velocity. L_Q/L_{tot} is the time (or length) fraction satisfying the Q^- criterion. The velocities are reduced to zero mean before processing.

$y^+_{min} > 20$, contained in the wider parallel band above the diagonal in figure 2(*a*). The p.d.f. of the objects in that family depends only on their vertical size, not on their distance from the wall, so that $p(y_{min}, y_{max}) \approx p(\Delta_y)$. By definition, $y_{min} \leqslant h$, and the detached Q^-s only rise modestly above the channel centre. The attached family, on the other hand, contains very large Q^-s that cross deeply into the opposite half of the channel. They are not easy to see in figure 2(*a*) because they are contained in the narrow band of very small y_{min}, but some of them reach almost to the opposite wall, $y_{max} \approx 2h$. For both Reynolds numbers, the number of attached Q2s and Q4s is about 40 % of the total number of Q^-s, but they are large enough to account for ∼80 % of their volume. There are very few attached Q1s and Q3s. They only account for about 7 % of the total number of Q^+s, and for 2 % of their volume. The numerical and volume fractions for the different kinds of Qs are summarized in table 2.

3.1. *Detached structures*

A similar separation was reported for clusters by del Álamo *et al.* (2006). In that case, the attached clusters are energy-containing eddies, while the detached ones are dissipative objects with sizes of the order of a few local Kolmogorov scales. Figure 2(*a*) suggests that the same is true for the detached Q^-s, because the width of their p.d.f.s appears to scale in wall units. In fact, the circumscribed boxes of the detached Qs are roughly cubical, with sides of the order of 30η at our Reynolds numbers. That does not necessarily mean that the Qs are isotropic. A characterization of the shape of the objects in terms of their smallest, intermediate and largest

dimensions will be introduced in §5. For the detached Qs, they are of the order of $7 \times 14 \times 45$ Kolmogorov units, suggesting that they are isotropically oriented, rather than isotropically shaped. Those sizes change relatively little from $H = 1$ to $H = 1.75$, and make the detached Qs comparable to fragments of the compact 'worms' in the dissipative ranges of isotropic turbulence (Jiménez *et al.* 1993) and channels (Tanahashi *et al.* 2004). It is clear, for example, that isotropic turbulence must have Reynolds-stress fluctuations, even if they cancel in the mean, and figure 1(*b*) shows that, even in channels, the standard deviation of τ is 2.5 times larger than its average. The figures just discussed suggest that the detached Qs are examples of those fluctuations. For example, figure 2(*b*) includes the fraction of the total Reynolds stress carried by the detached Qs. It is never large, and the contribution of the Q^+s essentially cancels that of the Q^-s.

The isotropic orientation of the detached Qs is consistent with the classical Corrsin (1958) criterion that eddies are isotropically oriented when their internal gradients are larger than the mean shear, $\ell^{-1} (\epsilon \ell)^{1/3} \gtrsim \partial_y \overline{u}$. If we estimate ϵ in terms of the production, eddies smaller than about $\ell_C = u_\tau / \partial_y \overline{u}$ should be isotropic. In the logarithmic layer, that implies $\ell_C \approx \kappa y$. The question was studied experimentally by Saddoughi & Veeravalli (1994), who concluded that the actual threshold for the Reynolds stress tensor to be approximately isotropic is $\ell_C \approx 0.25y$, implying that only attached structures of size $O(y)$ need to be examined to understand momentum transfer. We will indeed see in the next section that attached objects are responsible for most of the mean Reynolds stress.

Table 3 compares the characteristics of the Reynolds-stress fluctuations in several flows, most at considerably higher Reynolds numbers than ours. It turns out that the rough equality $\tau' \approx u'v'$ holds in all cases, including the plane jets for which the mean Reynolds stress is very small and countergradient. The correlation between u and v is responsible for the non-zero mean stress in the wall-bounded cases, but it is low enough to act as a second-order effect from the point of view of the intensity of the fluctuations of τ. Antonia & Atkinson (1973) and Lu & Willmarth (1973) showed that the p.d.f. of τ can be modelled as a joint Gaussian distribution of u and v, with the correct correlation coefficient. The resulting distribution is very intermittent, but its standard deviation differs little from $u'v'$ if $|\overline{\tau}|/u'v' \lesssim 0.5$.

The experiments in the table are one-dimensional hot-wire traces, and the dimensions of their Q^-s are estimated from the lengths of the segments in which $\tau > Hu'v'$, discarding segments shorter than 8η to make them comparable with the threshold for small objects used in the numerical channels. The results given in the table for the channels were obtained by mimicking the experimental procedure, intersecting the Qs detected in the previous section with random streamwise lines. The average dimensions of the structures in the atmospheric surface layer (ASL) are longer than in the jets, probably because they include attached objects that cannot be distinguished in the experimental traces. To clarify that effect, the experiments in the L2000 channel were repeated taking into account either all the Q^-s, or only the detached ones, which are probably more representative of the case of the jets. The average lengths of the detached Q^-s are shorter than when all the Q^-s are taken into account, but the effect is weaker than the difference between the ASL and the jets.

Even with those uncertainties, it is clear that the lengths of the Q^-s do not scale in Kolmogorov units. The closest match is the Taylor microscale λ, specially for the lower Reynolds numbers. That would be difficult to interpret, because the dynamical meaning of λ is unclear, but we will see below that it is the result of trying to define
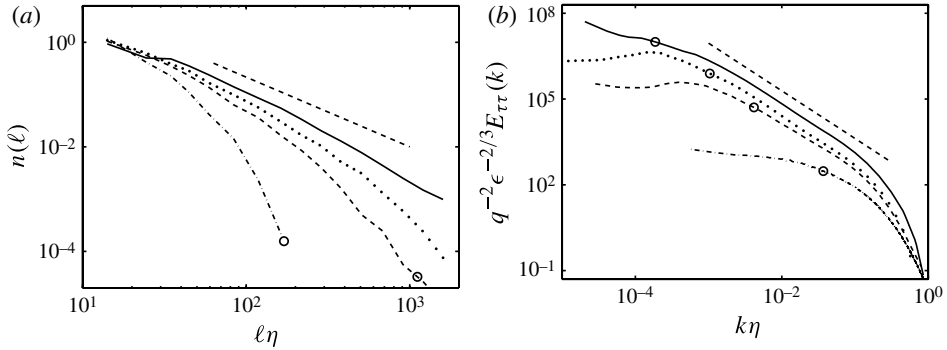
FIGURE 3. (*a*) Histograms of the lengths of the Q⁻s, measured along streamwise lines. $-\!-\!-\!-\!-$, L2000; $-\!-\!-$, round jet; . . . . . ., PJ2; ——, ASL. The slope of the dashed diagonal is $-4/3$. All the histogram are normalized with their value at $\ell = 15\eta$ to compensate for the truncation of the smaller objects. (*b*) Spectra of the $\tau = -uv$ product. Lines as in (*a*). The slope of the dashed diagonal is $-5/3$. The open circles in both figures mark the integral scale, L_ϵ/η.

a single length scale for a turbulent phenomenon. Figure 3(*a*) displays histograms for the lengths of the one-dimensional Q-intersections for the experimental and numerical cases. They are very wide, with maxima near $\ell \approx 10\eta$ in the two cases in which the resolution is enough to capture that range of scales (L2000 and ASL). To facilitate comparisons, all the histogram have been redrawn on identical logarithmic bins, starting from $\ell = 10\eta$, and normalized to unity in the first bin. They have tails reaching into the integral length scales, which are marked in both panels of figure 3, even if the spectra in figure 3(*b*) suggest that the sample length of the ASL is not enough to capture the longest structures. The best approximation to the histograms is a power law $n(\ell) \propto \ell^{-\alpha}$, with α between 4/3 and 5/3, approaching the former for high Reynolds numbers. The resulting average length is then

$$\overline{\ell} = \frac{\displaystyle\int n(\ell)\ell\, \mathrm{d}\ell}{\displaystyle\int n(\ell)\, \mathrm{d}\ell}, \tag{3.1}$$

where the two integrals extend over an inertial range of the order of $\eta < \ell < L_\epsilon$. The integral in the numerator is dominated by its upper limit, and is proportional to $L_\epsilon^{2-\alpha}$. The one in the denominator is dominated by its lower limit, and is proportional to $\eta^{1-\alpha}$. The mean length is $\overline{\ell} \propto L_\epsilon^{2-\alpha}\eta^{\alpha-1}$. For $\alpha = 5/3$, that average is proportional to $\lambda \propto (L_\epsilon\eta^2)^{1/3}$, which is the best fit for the lower-Reynolds number data in table 3, while for $\alpha = 4/3$ it is proportional to $(L_\epsilon\lambda)^{1/2}$, which grows somewhat faster, and may be a better fit for the higher Reynolds numbers. From their derivations, it is clear that neither average should be considered the length of a 'typical' object.

   The form of the ℓ histograms can be related to the spectrum of τ, reinforcing the argument that the objects that we are discussing are the carriers of the Reynolds-stress fluctuations. If we assume, from the previous discussion, that those fluctuations are objects with intensities of the order of the large-scale velocity q, and simplify them to a distribution of segments in which either $\tau = \pm q^2$ or $\tau = 0$, the correlation function $R_{\tau\tau}(r)$ is proportional to the probability that a point falls within an active segment

with $\ell > r$. For $\alpha = 4/3$, it can be estimated as

$$R_{\tau\tau}(0) - R_{\tau\tau}(r) \propto \int_0^r n(\ell)\ell \, d\ell \propto r^{2/3}, \tag{3.2}$$

corresponding to a spectrum $E_{\tau\tau}(k) \propto k^{-5/3}$. From purely dimensional arguments, the spectrum of τ would be expected to behave as $\epsilon^{4/3}k^{-7/3}$, but figure 3(b) shows that is not the case. The higher-order spectra of u^n were documented, among others, by Van Atta & Wyngaard (1975), who found them to behave as $k^{-5/3}$ for all orders. They gave theoretical arguments for the failure of the naive dimensional scaling, which are essentially that large- and small-scale quantities are statistically independent, and that the second-order structure function of the increments $\overline{\delta\,(u^n)^2}$ is dominated by terms of the form $u^{2n-2}\overline{\delta\,(u)^2}$. For example, the spectrum of quadratic quantities such as u^2 has the form $q^2\epsilon^{2/3}k^{-5/3}$. During the preparation of the present paper, Y. Kaneda (private communication) noted that the same argument should hold for the second-order quantity τ, and we have used that normalization in figure 3(b).

3.2. *Attached structures*

Attached Q⁻s are responsible for around 60 % of the total Reynolds stresses in both channels, even if they cover less than 8 % of the total area at all heights. As expected, their contribution in terms of volume and tangential Reynolds stresses increases as H is lowered. At the same time, there is a transfer from detached to attached objects, reflecting the percolation process by which small detached units collect into larger attached ones. For example, the percentage of detached volume with respect to the total Q⁻s changes from 60 % at $H = 3$, to 14 % at $H = 1$. Interestingly, the percolation does not proceed at the same pace for the different kinds of structures. While the detached volume fraction of Q4s changes little from $H = 1.75$ to $H = 1$, suggesting that their percolation is essentially complete, that of the Q2s decreases by 30 % in the same range.

The contributions to the mean stress mentioned above are in good agreement with those reported in the literature. Figure 6 in Willmarth & Lu (1972) shows that the contribution from Q2s and Q4s to the total Reynolds stresses in the buffer region is ∼60 % when $\widetilde{H} \approx 4.5$ ($H \approx 1.75$), and that those Qs cover roughly 10 % of the measurements. At the lower end of the logarithmic region, Ganapathisubramani *et al.* (2003) report that hairpin packet signatures covering 4 % of the total area contribute about 28 % of the Reynolds stresses, which also agrees with our data for $H = 3$ (not shown). Narasimha *et al.* (2007) report that $\widehat{H} = 1$ yields structures that contains 100 % of the total Reynolds stresses, while covering roughly 50 % of the measurement time in the neutral atmospheric boundary layer at $h^+ \sim 10^7$ ($y^+ \sim 10^5$). When we use $H = 1$ ($\widehat{H} \approx 0.9$), the contribution to the total Reynolds stresses from attached Qs is also about 90 %, but they only fill 20 % of the area. The difference in covered area is most likely due to the eduction scheme used by Narasimha *et al.* (2007), who identify the structures by means of $\widehat{H}$, but subsequently extend them to the nearest zero crossing of the Reynolds stress. Note that the covering fractions given in table 3 for our channels are in reasonable agreement with those for the other high-*Re* flows, suggesting that *Re* number effects can not explain the aforementioned difference between our results and Narasimha *et al.* (2007).

The contribution from the different quadrants, at $H = 0$, has been treated extensively in the literature, and was discussed in some detail by Jiménez *et al.* (2010) in the context of the similarities and differences between internal and external shear flows.
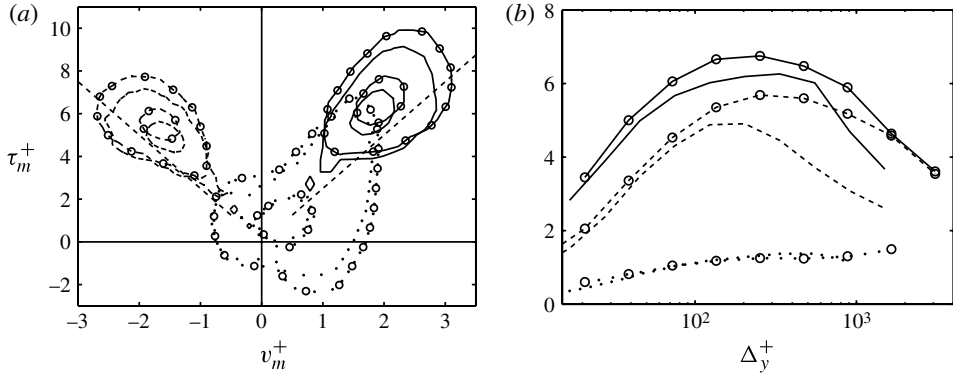
FIGURE 4. (*a*) Joint p.d.f. of the wall-normal velocities and the tangential Reynolds stresses averaged over individual attached objects with Δ_y in the logarithmic layer. For each case, the plotted contours contain 50 and 98 % of the data. The straight dashed lines are $\tau_m^+ = \pm 2.5 v_m^+$. (*b*) Mean τ_m^+ for the different objects, as functions of their heights. In both panels, ——, Q2; ---, Q4; ......, clusters. Lines without symbols are L950; those with symbols are L2000.

The reader is referred to that discussion for further details and references, but the behaviour is roughly as in figure 2(*b*), including the reversal of the roles of Q2s and Q4s in the buffer layer, and the decay of the contribution of the Q4s far from the wall.

The picture that emerges from the previous discussion is that relatively few (25–30 % by number), large and intense wall-attached Q^-s are responsible for most of the momentum transfer, while detached Qs play a secondary role. From now on, we will focus on the geometry and structure of the attached Q^-s, including their spatial distribution, their associated velocity fields, and their relationship with vortex clusters.

4. Size and intensity of the attached Q^-s

The averaged Reynolds stress of an object, τ_m, is defined in the same way as the averaged velocities in (2.2), and is a measure of its intensity. Figure 4(*a*) shows the joint p.d.f. of v_m and τ_m for the attached Q^-s of the logarithmic layer. It clearly separates into Q2s, with $v_m > 0$, and Q4s with $v_m < 0$, confirming that the classification of the Qs in terms of their averaged velocities is meaningful. Similar plots are obtained in the buffer and outer regions, or using u_m instead of v_m.

The p.d.f.s of both kinds of Q^-s are roughly aligned along $\tau_m^+ = 2.5|v_m^+|$, which is consistent with a simple mixing-length argument in which the Reynolds stress is generated by displacing the mean velocity profile by an amount proportional to the eddy size, $l \propto y$. In the logarithmic region, $\partial_y \overline{u} \approx u_\tau / \kappa y$, and

$$\tau^+ \propto v^+ (l \partial_y \overline{u})^+ \propto v^+. \tag{4.1}$$

This is a very rough estimate, but it provides a simple explanation for the other interesting feature of figure 4(*a*), which is that the Reynolds stresses of the Q4s are weaker than those of the Q2s with the same $|v_m|$, probably because they can only draw momentum from the flatter shear in the central part of the channel (see figures 2*b* and 4*b*). The asymmetry between sweeps and ejections has been known for a long time (Nakagawa & Nezu 1977), and its modelling has been discussed often. The best-known argument is based on the skewness of the velocity fluctuations (Raupach 1981; Katul *et al.* 2006), but it was shown by Jiménez & Hoyas (2008) that
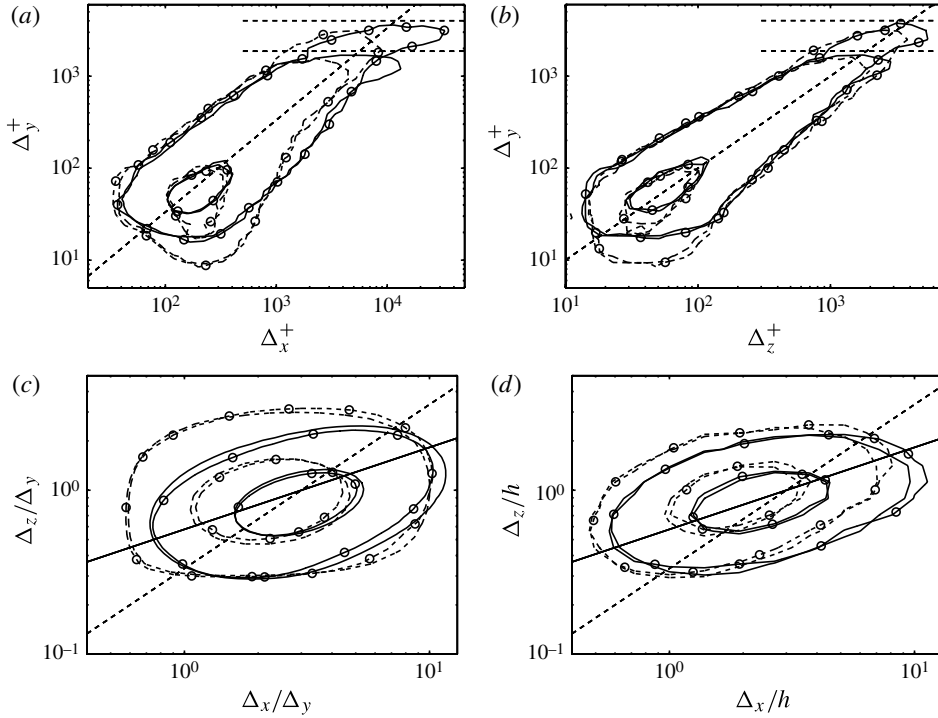
FIGURE 5. Joint p.d.f.s of the logarithms of the sizes of the boxes circumscribing attached Q^-s. (a) $p(\Delta_x^+, \Delta_y^+)$. (b) $p(\Delta_z^+, \Delta_y^+)$. (c) $p(\Delta_x/\Delta_y, \Delta_z/\Delta_y)$ for objects in the logarithmic layer. (d) $p(\Delta_x/h, \Delta_z/h)$ for objects with $0.5h < \Delta_y < 0.95h$. In all figures, the contours plotted contain 50 and 98 % of the p.d.f. ——, Q2s; – – –, Q4s. Lines without symbols are L950, and those with circles are L2000. In all the panels, the solid and dashed straight lines are $\Delta_x\Delta_y = 3\Delta_z^2$ and $\Delta_x = 3\Delta_z = 3\Delta_y$, respectively, and the horizontal dashed ones are $2h$.

the velocity skewness can itself be traced to the inhomogeneity of the mean velocity profile.

Figure 4(a) includes the p.d.f. of the vortex clusters, and shows that most of them are Q2s, in agreement with the conditional velocity fields of del Álamo *et al.* (2006). On the other hand, a non-negligible fraction of clusters lie in other quadrants: 14 % are Q4s, 5 % are Q1s and 1 % are Q3s, showing that their association with the Q2s is not exclusive. Accordingly, the averaged stress integrated over the attached clusters in figure 4(b) is weaker than for the Qs.

Figure 5 shows the p.d.f.s of the logarithms of the sizes of the circumscribing boxes for the Q^-s, $p(\Delta_x, \Delta_y)$ and $p(\Delta_z, \Delta_y)$. They follow fairly well-defined linear laws,

$$\Delta_x \approx 3\Delta_y \quad \text{and} \quad \Delta_z \approx \Delta_y, \tag{4.2}$$

except for objects with $\Delta_y \gtrsim 1$, crossing the central plane. del Álamo *et al.* (2006) reported similar, although slightly wider, laws for the attached clusters, $\Delta_z \approx 1.5\Delta_y$.

Figure 5 shows that the sizes of the boxes of the Q2s and Q4s are similar, but that the latter are more common below $\Delta_y^+ = 20$, which is to be expected because their negative v_m tends to flatten them against the wall. Those flattened Q4s have widths comparable to the high-speed streaks reported by Jiménez, del Álamo & Flores (2004) in the buffer region, but they are shorter, in agreement with the conclusion in that

paper that both the high- and the low-velocity streaks of the buffer layer are composite objects.

There are other, smaller, differences between the size distributions of Q2s and Q4s. Figure 5(*c*) shows that the Q2s are longer and narrower than the Q4s in the logarithmic region, and the same is true in figure 5(*d*) for the outer layer, although to a lesser degree. It is interesting that, although the modes of the size distributions grow linearly with y, as shown in figures 5(*a*) and 5(*b*), the relationship between Δ_x and Δ_z in the distributions at a fixed Δ_y is not linear. Both p.d.f.s are roughly aligned along $\Delta_x \Delta_y \propto \Delta_z^2$, which recalls the shape of the streamwise energy spectra in del Álamo *et al.* (2004). However, the two behaviours are probably unrelated, and it is even unclear whether the alignments in figures 5(*c*) and 5(*d*) are quadratic or some similar power. What those p.d.f.s measure is the dispersion among the sizes of structures with similar Δ_y, and the nonlinear alignment implies that there is more variation in Δ_x than in Δ_z. However, the dispersion is not large, and its amplitude does not appear to vary with the Reynolds number, making the definition, and relevance, of a power law uncertain. Most probably, the message of figures 5(*c*) and 5(*d*) is just that the mechanisms that deform the structures along the two coordinates are different. A possible model is that the deformation along x is due to the shear, while the weaker dispersion by the background turbulence is responsible for the spanwise growth (Flores & Jiménez 2010*b*). On the other hand, an explanation in terms of longitudinally growing vortex packets may be equally valid (Tomkins & Adrian 2003), and it would be difficult to distinguish between the two models, or others, until time-resolved evolutions are analysed.

The 'overhangs' of the p.d.f.s in figures 5(*a*) and 5(*b*) contain the largest structures, which are mostly Q2s extending beyond the centreline. Their sizes, $\Delta_x \approx 20h$ and $\Delta_z \approx 2h$, are comparable to the very-large-scale motions of Jiménez (1998) and Kim & Adrian (1999), or to the global modes of del Álamo *et al.* (2004). They are the only parts of the p.d.f.s that change appreciably with the detection threshold H, and also the only ones that do not satisfy the scaling self-similarity of the smaller objects, suggesting that the global modes are different from the Qs of the logarithmic and buffer layer, and are probably formed by percolated juxtapositions of smaller subunits. Figure 8 includes examples of a cluster and a Q2 from the logarithmic layer, and of a global Q2, and highlights the differences among them. The appearance of the latter clearly suggests a composite character, and it is difficult not to remark its similarity with the large-scale low-velocity streaky structures discussed, for example, by Hutchins & Marusic (2007*a*), or in figure 4 of Flores *et al.* (2007).

The very-large outer objects extending to the centre of the channel carry a substantial fraction of the Reynolds stresses (Jiménez *et al.* 2004; Guala, Hommema & Adrian 2006; Balakumar & Adrian 2007). Figure 6 shows how the total stress carried by the Q^-s is distributed among objects of different heights. In general, the stress carried by objects of height y_{max} is maximum near $y = y_{max}/3$, although the distributions are not strictly self-similar, and tend to peak closer to the wall for the Q4s than for the Q2s. It is striking that about one third of the stress carried by the attached Q^-s is due to objects crossing the centreline. About 70 % of those objects are Q2s, and the rest are Q4s. The former are larger, accounting for 90 % of the volume. There are only about 50 very large objects per field ($<1\%$), but they account for about 60 % of the volume of the attached Qs, or 4 % of the volume of the channel.

To check which fraction of the smaller attached structures are also aggregates of even smaller ones, we analyse the fragmentation of the Q^- as the threshold varies from $H = 1.75$ to $H = 3.0$ by tracking the Cartesian boxes circumscribing them.
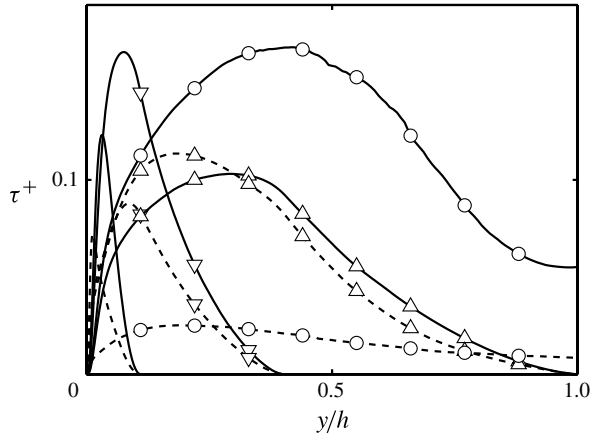
FIGURE 6. Reynolds stress carried by attached Q2s and Q4s with heights in different bands. Case L950. Lines without symbols, $y^+_{max} < 100$; $\triangledown$, $100\nu/u_\tau < y_{max} < 0.4h$; $\triangle$, $0.4h < y_{max} < h$; $\circ$, $y_{max} > h$. Solid lines are Q2s, dashed ones are Q4s.

Intersections of actual objects are forbidden by the clustering procedure, which collects intersecting objects into single ones, but the boxes may intersect each other, usually because a large attached Q overlies smaller ones near its base. Those intersections are not very relevant, and usually involve objects of very different heights. To avoid them, only boxes whose heights differ by less than a factor of two,

$$1/2 \leqslant \Delta_y^{(i)}/\Delta_y^{(j)} \leqslant 2, \tag{4.3}$$

are considered as interacting in the rest of this paper. Boxes with no interactions when $H = 1.75$, and therefore presumably 'isolated' (ranging from 90 % by number in the buffer layer to 50 % above $0.2h$), were tracked when the threshold was increased to $H = 3$. Of those that survived (~ 35 %), most were still isolated at the higher threshold, but the rest broke into sub-boxes, and were considered to have been originally composite. The number of composite Q$^-$s, and the number of pieces, increases with the distance to the wall; from 10 %, and an average of 2.2 fragments for boxes originally below $y^+_{max} = 100$, to 20 % and an average of 2.5 fragments when $y^+_{max} > 0.2h$.

Those percentages depend little on the Reynolds number, but change when the limit in (4.3) is relaxed from 2 to 4, allowing a wider range of scales between an object and its fragments. In that case, the percentage of initially isolated objects ranges from 90 % below $y^+_{max} = 100$ to only 15 % above $y^+_{max} = 0.2h$, and the fraction of surviving Q$^-$s increases to almost 60 % away from the wall. Not surprisingly, more of those surviving objects turn out to be composite, ranging from 10 % near the wall to 40 % above $0.2h$.

We can now compare the size distributions of the Q$^-$s with other scaling information about wall-bounded flows. The proportionality $\Delta_z \approx \Delta_y$ in (4.2) agrees approximately with the results of Tomkins & Adrian (2003) and Ganapathisubramani *et al.* (2003) for hairpin packets in the near-wall region. It should be stressed that the Qs studied here cover the entire height of the flow, from $\Delta_y^+ \approx 10$ to $\Delta_y = 2h$, while ordered hairpin packets have only been observed directly in the buffer and lower logarithmic layers ($y^+ \lesssim 200$), and become disorganized further from the wall (Lee & Sung 2011; Jiménez 2012).
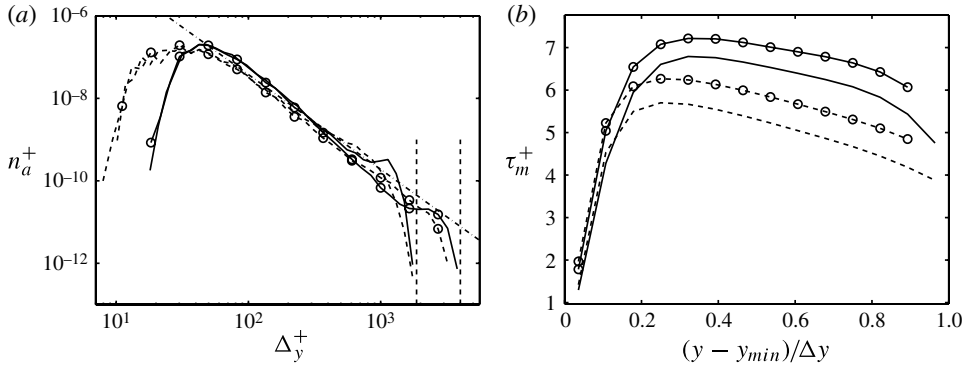
FIGURE 7. (*a*) Number n_a^+ of attached events per unit height and wall area, in wall units. ——, Q2s; – – –, Q4s. Lines without symbols are L950, those with circles are L2000. The chaindotted line is $n_a \propto \Delta_y^{-2}$, and the two vertical dashed lines are $\Delta_y = 2h$. (*b*) Mean $\tau_m(y)$ of attached Q⁻s in the logarithmic layer, as a function of *y* within the object. ——, Q2; – – –, Q4. Lines without symbols are L950, those with circles are L2000.

del Álamo *et al.* (2004) and Hoyas & Jiménez (2006) found that the peaks of the *uv*-cospectrum of L950 and L2000 align along $\lambda_z \approx 3y$, which agrees with (4.2) if we accept, from figure 6, that the maximum stress of the Q⁻s is at $y \approx \Delta_y/3$. It also agrees with the relation between the width of the minimal logarithmic boxes in Flores & Jiménez (2010*a*) and the height to which they maintain turbulence. Moreover, the proportionality $\Delta_x \approx 3\Delta_z$ in (4.2) implies that the peak of the *uv*-cospectrum should be around $\lambda_x \approx 9y$, which is not too far from the ratio, $\lambda_x/y \approx 10$–15, found by Jiménez & Hoyas (2008) in boundary layers and channels. In all, those figures reinforce the conclusion that the structures described here are those responsible for most of the Reynolds stresses in wall-bounded turbulent flows.

The *y* dependence of the number of attached Q⁻s per unit height and wall area is given in figure 7(*a*). As we have already seen, Q4s reach closer to the wall than Q2s, but otherwise their densities are similar and decay with size as $n_a^+ \propto (\Delta_y^+)^{-2}$. Because the cross-sections of individual Q⁻s are proportional to $\Delta_x \Delta_z \propto \Delta_y^2$, the fraction of the area covered by Q⁻s at a given *y* within the logarithmic layer is equally distributed among the Δ_y of the Q⁻s crossing that level, which are those with $\Delta_y > y$. Moreover, since the Reynolds stress averaged over the section of individual Q⁻s is also remarkably uniform within each structure, as shown in figure 7(*b*), the uniform distribution of areas implies a uniform contribution to the overall Reynolds stress by each Δ_y. Integrating over $y < \Delta_y < h$, the total stress is proportional to $h - y$, in agreement with the constant fraction of the total stress carried by the Q⁻s in figure 2(*b*). Note that some such constraint has to be satisfied by any set of structures carrying the bulk of the Reynolds stress across the channel, because the total stress is fixed by the mean momentum equation. It implicitly determines the decay law for n_a

On the other hand, the clusters, which are not constrained by the dynamics to carry a constant property flux, decay faster with Δ_y than the Q⁻s. del Álamo *et al.* (2006) showed that their density behaves like $n_c^+ \propto (\Delta_y^+)^{-3}$. As a consequence, attached clusters are essentially near-wall objects, which can only associate with the smaller Q⁻s. We will see in §6 that the larger Q⁻s are mostly independent of small-scale vorticity.
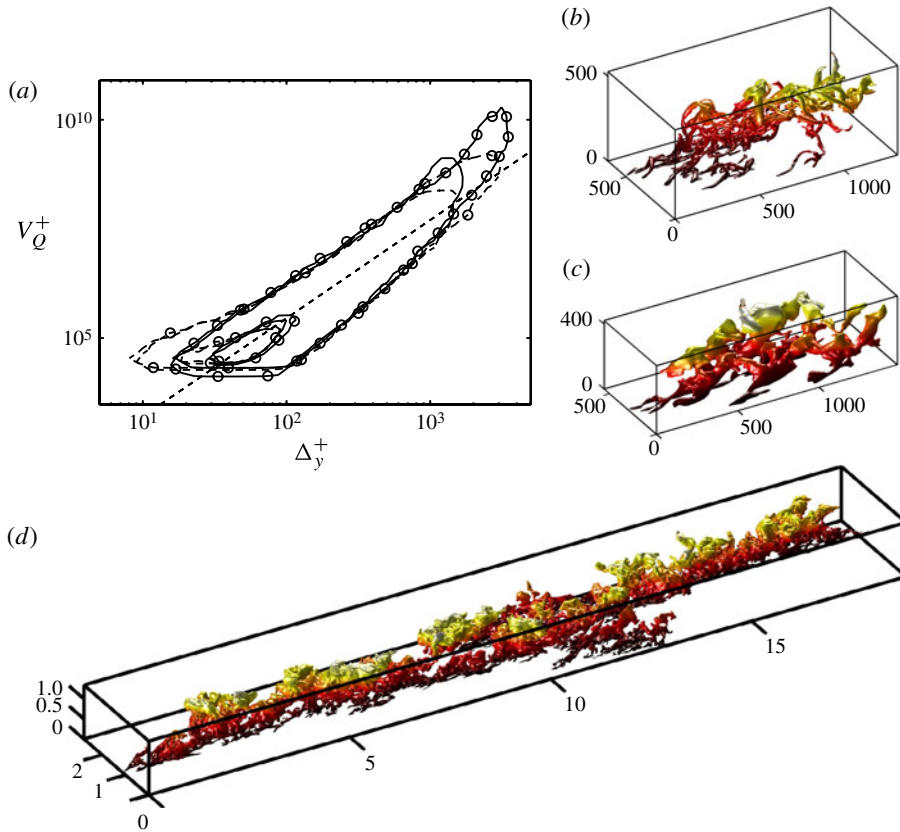
FIGURE 8. (Colour online available at journals.cambridge.org/flm) (*a*) Joint p.d.f. of the logarithms of the volume V_Q and the height Δ_y of attached Q^-s. The contours contain 50 and 98 % of the data. The dashed straight line is $V_Q \propto \Delta_y^{2.25}$. (*b*) Instantaneous visualization of an attached cluster. (*c*) Instantaneous visualization of an attached Q2. The axes of (*b*) and (*c*) are in wall units. (*d*) Very-large-scale attached Q2, with the axes scaled with *h*. Note that the object crosses the centre of the channel. The visualizations are coloured with the distance to the wall; red (dark) near the wall, and white near the top. Flow is from bottom-left to top-right.

5. Shape of individual objects

We showed in the previous section that, at least in the logarithmic layer, the circumscribing boxes of the attached Q^-s form a self-similar family with sizes proportional to *y*. The same was shown for the vortex clusters by del Álamo *et al.* (2006). In this section we study the shape of the objects themselves.

Figure 8(*a*) is the joint p.d.f. of the volumes and heights of the attached Q^-s, and follows quite well $V_Q^+ \propto (\Delta_y^+)^\alpha$, with $\alpha \approx 2.25$. A similar law, with $\alpha \approx 2$ was found for the clusters by del Álamo *et al.* (2006), who interpreted it as an estimate of their fractal dimension, and as an indication that they were shell-like. Figure 8(*a*) implies that the Qs have slightly fuller shapes, which is confirmed by inspection of the individual cluster and Q2s in figure 8(*b–d*).

Although the power law in figure 8(*a*) seems persuasive, it can only be related to a fractal dimension by assuming that the objects themselves are self-similar. A
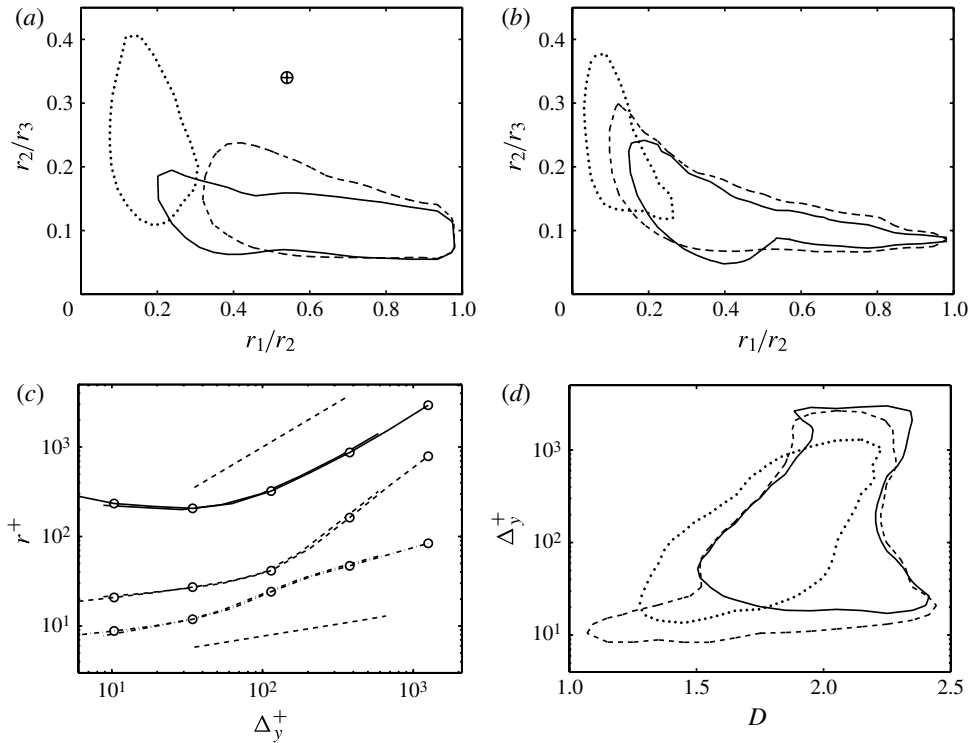
FIGURE 9. (*a*) P.d.f.s of the aspect ratios r_1/r_2 and r_2/r_3 for attached Q⁻s. ——, Buffer layer; – – –, logarithmic; ......, outer. Probability contours include 50 % of the data. ⊕, average aspect ratios of the detached Qs. (*b*) As in (*a*), for attached clusters. (*c*) Intrinsic lengths of the attached Qs. – – – – –, r_1; – – –, r_2; ——, r_3. Lines with symbols are L2000; those without symbols are L950. The lower dashed straight line is 3η, and the upper one $10\Delta_y$. (*d*) Joint histogram of the fractal dimension and Δ_y^+, normalized with the maximum at each Δ_y. ——, Q2; – – –, Q4, ...; clusters. Probability contours include 90 % of the data. Figures (*a*), (*b*) and (*d*) are L2000.

more direct characterization requires estimating the shapes of the individual structures, to which end we define three 'intrinsic' lengths for each object, following the methodology of Moisy & Jiménez (2004). The outer scale, r_3, is the size of the smallest circumscribing cube, which typically coincides with Δ_x. The inner scale, r_1, is the side of the largest inscribed cube, and is computed from the inner coverage fraction, as in the appendix in Moisy & Jiménez (2004). The third scale, r_2, is related to the volume by $V_Q = r_1 r_2 r_3$.

The inner length, r_1, estimates the 'thickness' of the object, and is always the smallest of the three. For smooth objects, one also expects that $r_1 \leqslant r_2 \leqslant r_3$, and the two aspect ratios (r_1/r_2, r_2/r_3) give an idea of the shape of the object. Ideal spheres, tubes, sheets and ribbons have aspect ratios of the order of $(1, 1)$, $(1, 0)$, $(0, 1)$ and $(0, 0)$, respectively (Moisy & Jiménez 2004), but the shapes of non-smooth objects can be very different from those ideal ones. For example, it is not always true that $r_2 < r_3$, even approximately, as can be seen by considering a large piece of cloth packed into a small box. The ratio r_2/r_3 characterizes the amount of 'wrinkling' of the object, but there are relatively few cases among our Q⁻s and clusters in which the smooth ordering is not satisfied. The p.d.f.s of the aspect ratios for the attached Q⁻s and

clusters are shown in figures 9(*a*) and 9(*b*), respectively. Both types of objects change from being tubes or ribbons in the buffer and lower logarithmic layers, to fuller sheets in the centre of the channel, although the somewhat larger values of r_1/r_2 of the Qs confirm their slightly fuller shapes.

We gave in §3 typical intrinsic lengths for the detached Qs, which were of the order of the Kolmogorov scale, presumably making them smooth objects. Their aspect ratios, $(r_1/r_2, r_2/r_3) \approx (0.5, 0.3)$, put them in the class of elongated ellipsoids, or 'flakes', fuller than the attached Q^-s or clusters (figure 9*a*).

Figure 9(*c*) shows the evolution with height of the average lengths of the attached Q^-s. Somewhat surprisingly, the inner length, $r_1/\eta \approx 5$–15, is of the order of the local Kolmogorov scale, suggesting that even these larger structures of a large-scale quantity, such as the Reynolds stress, are shells formed from viscous-scale subunits. The ratio r_1/η increases slowly with the distance from the wall, and it can be shown that its probability distribution is fairly narrow at each wall distance, as opposed to the wide tails of figure 3(*a*). The other two lengths grow approximately linearly with *y*, except in the buffer layer. The largest one, $r_3 \approx 2.5\Delta_y$, agrees roughly with Δ_x in the logarithmic layer, but the intermediate one, $r_2 \approx 0.5\Delta_y$, is smaller than Δ_z. The implied shapes change from tubes, or narrow ribbons, in the buffer layer, to increasingly wrinkled sheets away from the wall. They are moderately elongated streamwise, of sizes of the order of the integral scale, but their small, perhaps viscous, thickness suggests that they are formed by connecting subunits similar to the detached Qs.

The ratio r_2/r_3 increases with increasing *y*, suggesting that the wrinkling increases with increasing size, as expected. That was confirmed by counting the number of discrete intersections (n_I) of random lines aligned with each coordinate axis within the circumscribing boxes of individual objects. It turns out to be proportional to $\Delta_y^{+1/2}$ along the three coordinate axes, implying mean distances between intersections of the order of $\Delta_y^{+1/2} \propto \lambda^+$. That recalls the scaling of the detached Qs discussed in §3.1, and probably has a similar origin. In fact, if the volume of each subunit is estimated by dividing the total volume of the Qs, which is proportional to $\Delta_y^{+2.25}$, by n_I^3, the result is $\Delta_y^{+0.75} \propto \eta^{+3}$, which is consistent with the dimensions given above for the detached objects. The resulting model for the attached Qs is a sponge-like object formed by the agglutination of ellipsoidal flakes similar to the detached Q, most of which are of the order of the Kolmogorov scale, but which span a wide range of sizes. The examples shown in figure 8(*c–d*) support this model of a 'sponge of flakes', in the same way that figure 8(*b*) suggests that vortex clusters are 'sponges of strings'.

Following Moisy & Jiménez (2004), the fractal dimension of individual objects can be statistically estimated by box counting within their bounding boxes. Each object is circumscribed within a cube of side r_3, which is then divided into smaller cubes of size *r*. The number $N(r)$ of cubes containing at least one point of the object is then counted. If we can approximate $N(r) \propto r^{-D}$ for $r_1 < r < r_3$, the exponent *D* can be considered as the fractal dimension of the individual object.

Figure 9(*d*) shows the joint histogram of *D* and Δ_y, and is roughly consistent with the discussion above. The dimension increases slightly with the height of the Qs and clusters, with a wide distribution between $D = 1$ and $D = 2$ in the buffer layer, increasing towards $D \approx 2$ away from the wall. As above, the dimension of the clusters is slightly lower than for the Qs. The fractal dimension of the Qs suggests a shell, but we have just seen that it has to be a very corrugated one. Note that the dimensions in figure 9(*d*) are lower than those obtained above from the evolution of the volume
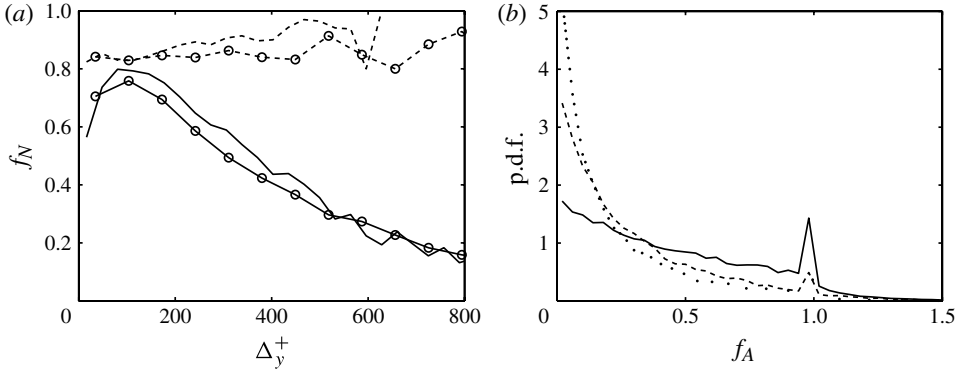
FIGURE 10. (*a*) Fraction of clusters (Q⁻s) whose boxes are intersected by one or more boxes of a Q⁻ (cluster), as function of their Δ_y. ——, Qs; –––, clusters. Lines without symbols are L950, those with symbols are L2000. (*b*) Probability density function of the fraction of the volume of cluster boxes that is filled by intersecting boxes of Q⁻s. Case L2000, for clusters in the logarithmic layer. ——, Q2s; –––, Q4s; . . . . . ., randomized Q⁻s.

with height. The reason is that the objects become thicker as they become taller. We showed in §2 that the Kolmogorov scale increases in the logarithmic layer as $y^{1/4}$. The volume of a 'sheet' of dimension D, with outer scale Δ_y and thickness η, is proportional to $\Delta_y^D \eta^{3-D}$. Substituting $\eta \propto \Delta_y^{1/4}$, we obtain $V_Q \propto \Delta_y^\alpha$, and

$$\alpha = \tfrac{3}{4}(D+1). \tag{5.1}$$

Taking, from figure 9(*d*), $D = 1.7$ for clusters, and $D = 2$ for Qs, we obtain $\alpha = 2$ and $\alpha = 2.25$, respectively, in reasonable agreement with the results of figure 8(*a*) for the Q⁻s, and of del Álamo *et al.* (2006) for the clusters.

Using a DNS of isotropic turbulence, Bermejo-Moreno & Pullin (2008) characterized the geometry of eddies of a passive scalar as blobs or tubes for the larger scales, and as sheets for the smaller ones, which could be construed as being related to the present results. However, beside referring to a different flow and variable, the Qs described here are conceptually different from the objects discussed by those authors. Our Qs coexist in physical space without intersecting each other, while they filter their fields before analysing them, with the result that their small-scale objects are engulfed within their large-scale ones. One of the conclusions of the discussion above should be that different small-scale quantities have different geometries (see also Moisy & Jiménez 2004), and our results and those of Bermejo-Moreno & Pullin (2008) are probably unrelated.

6. Spatial organization

We discuss now the relative positions of the objects characterized in the previous sections. Consider first the relation between clusters and Q2s, which were shown by del Álamo *et al.* (2006) to be statistical markers for each other. As in §4, we only consider that two objects are related if their heights differ by less than a factor of two.

Figure 10(*a*) shows that more than 80 % of the clusters intersect with at least one Q⁻, at all heights. The converse is not true, and the probability that a Q⁻ intersects a cluster is only high near the wall. It decays further up, together with the density of clusters, essentially because there are not enough tall clusters to cover all the tall Q⁻s.

Figure 10(*b*) contains the p.d.f.s of the fraction of the volume of the box of each attached cluster that is covered by boxes containing Q2s or Q4s, and addresses the question of how relevant are the intersections between Q⁻s and clusters. The figure is drawn for the logarithmic region of L2000, but similar results hold for L950 and for other heights. In theory, the intersected fraction f_A can be greater than one, because the boxes of the Qs may overlap, and some parts of the cluster can be covered by more than one Q. Figure 10(*b*) shows that the p.d.f.s drop sharply beyond $f_A = 1$, indicating that those cases are rare. Note that the discreet peak at $f_A = 1$ is an artifact of considering covering fractions. (Lets consider a system with two boxes A and B, where the relative positions of the boxes are random and where the box B is larger than box A. The probability of the box A being completely covered by box B ($f_A = 1$) is proportional to a triple-infinitude of relative positions. But the probability of any other covering fraction is proportional to a double-infinitude, the positions resulting of moving box B over the surface of box A.) It is clear from the figure that the intersections of clusters with Q2s are more probable than with Q4s, in agreement with figure 4(*b*). Moreover, to test whether those intersections are just a statistical consequence of the areas covered by the different objects, we recomputed their statistics after randomizing the x–z positions of the centres of the boxes of the Q⁻s. The resulting p.d.f. is very close to that of the Q4s, supporting the idea that their intersections with the clusters are mostly a matter of chance, while those of the Q2s are not.

We analyse next the relative positions of different objects, defining joint p.d.f.s, $p^{(ij)}(\delta_x, \delta_z)$, for the position of events of type j with respect to those of type i, where i and j are 2 for Q2s, 4 for Q4s and C for clusters. The relative distances

$$\delta_x = 2\frac{x^{(j)} - x^{(i)}}{d^{(j)} + d^{(i)}} \quad \text{and} \quad \delta_z = 2\frac{z^{(j)} - z^{(i)}}{d^{(j)} + d^{(i)}}, \quad (6.1)$$

are referenced to the position of i-objects, $(x^{(i)}, z^{(i)})$, and are normalized with the semi-sum of the wall-parallel diagonals of each pair of events,

$$d^{(i)} = \sqrt{\Delta_x^{(i)2} + \Delta_z^{(i)2}}. \quad (6.2)$$

The spanwise statistical symmetry of the flow allows us to choose the direction of the δ_z axis for each individual reference event. In p.d.f.s involving only Qs, such as figures 11(*a*), 11(*b*) and 11(*d*), $\delta_z > 0$ is chosen pointing to the nearest Q of different kind than the reference. For the p.d.f.s of the positions of clusters with respect to Qs, such as figures 11(*e*) and 11(*f*), $\delta_z > 0$ points towards the closest cluster. That choice weights the p.d.f.s towards the positive δ_z, but allows us to test the symmetry of individual groups of events. For example, if Q2s were typically surrounded by two roughly equivalent Q4s, as in a symmetric trio, the p.d.f. of the positions of Q4s with respect to Q2s would have a secondary peak with negative δ_z, in addition to the primary one with $\delta_z > 0$. Weaker secondary peaks correspond to statistically more one-sided associations.

Figure 11 shows the p.d.f.s for reference objects within the logarithmic region, with probability isolines normalized with $p_\infty^{(ij)}$, which is the averaged value of the p.d.f. for $\delta_x^2 + \delta_z^2 > 9$. The three distributions for pairs of objects of the same type, figure 11(*a*–*c*), show that they tend to be aligned in the streamwise direction, and that the objects do not overlap, as shown by the low probabilities at $\delta_x = 0$. The Q⁻s tend to be spaced longitudinally by $|\delta_x| \approx 1$, with the probability of finding another Q of the same kind in that position being more than twice the probability of finding it anywhere else. The
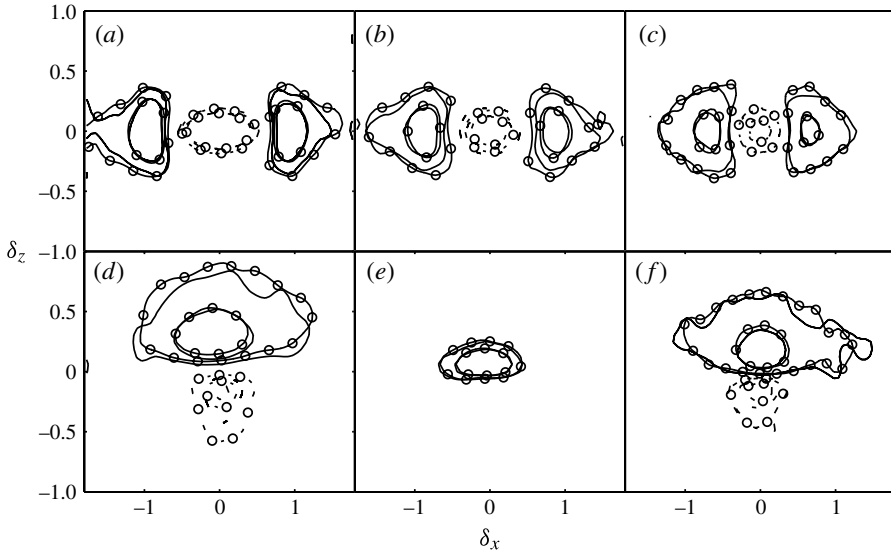
FIGURE 11. Probability density functions of the relative positions of clusters, Q2s and Q4s, using as reference events in the logarithmic layer: (*a*) p^{22}; (*b*) p^{44}; (*c*) p^{CC}; (*d*) p^{24}; (*e*) p^{2C}; (*f*) p^{4C}. Solid contours are $p^{(ij)}/p^{(ij)}_{\delta,\infty} = 1.5$ and 2. Dashed contours are $p^{(ij)}/p^{(ij)}_{\delta,\infty} = 0.66$ and 0.5. Lines without symbols are L950 and those with symbols are L2000.

clusters also align longitudinally, but tend to be a little closer than the Qs, $|\delta_x| \approx 0.75$. That means that they almost overlap each other, and is consistent with the discussion in the previous sections that the Qs are slightly fuller objects than the clusters.

Objects of different kinds tend to align spanwise, rather than streamwise. Figure 11(*d*) shows that the most probable position of the Q4s with respect to the Q2s is to one side of the Q2, and very close to it, suggesting that both events tend to form parallel pairs. Our choice of the sign of δ_z requires the closest Q4 to be at $\delta_z > 0$, but the lack of any peak at $\delta_z < 0$ (where the probability of finding a Q4 is actually lower than the average) strongly implies one-sided pairs, rather than symmetric hairpins. Although not shown, $p^{(42)}$ is similar to $p^{(24)}$, because the Q2s and Q4s have roughly the same density and size distribution throughout the logarithmic layer.

The p.d.f. of the relative position of the clusters with respect to the Q2s is presented in figure 11(*e*), and shows that they tend to be embedded within Q2s of similar sizes, in agreement with figure 4(*a*), and with the conditional velocity fields in del Álamo *et al.* (2006). Figure 11(*f*) reinforces that conclusion, because the clusters are in $\delta_z > 0$ with respect to the Q4s, which is also the preferred location of the Q2s.

The picture that emerges is one of spanwise pairs of Q2s and Q4s, with a cluster associated with the Q2, and with the groups aligned streamwise. The p.d.f.s in figure 11, including the existence of pairs and the streamwise distance between neighbouring Q^-s, are robust with respect to the eduction threshold. They change little in $1 < H < 3$, implying that the pairs are distinct units rather than random pieces of longer objects. The statistical evidence for pairs of Q2s and Q4s is also strong. Roughly 50 % of the Q^-s in the logarithmic region are involved in simple pairs, and 30 % are involved in more complicated trios or groupings. The rest are isolated.
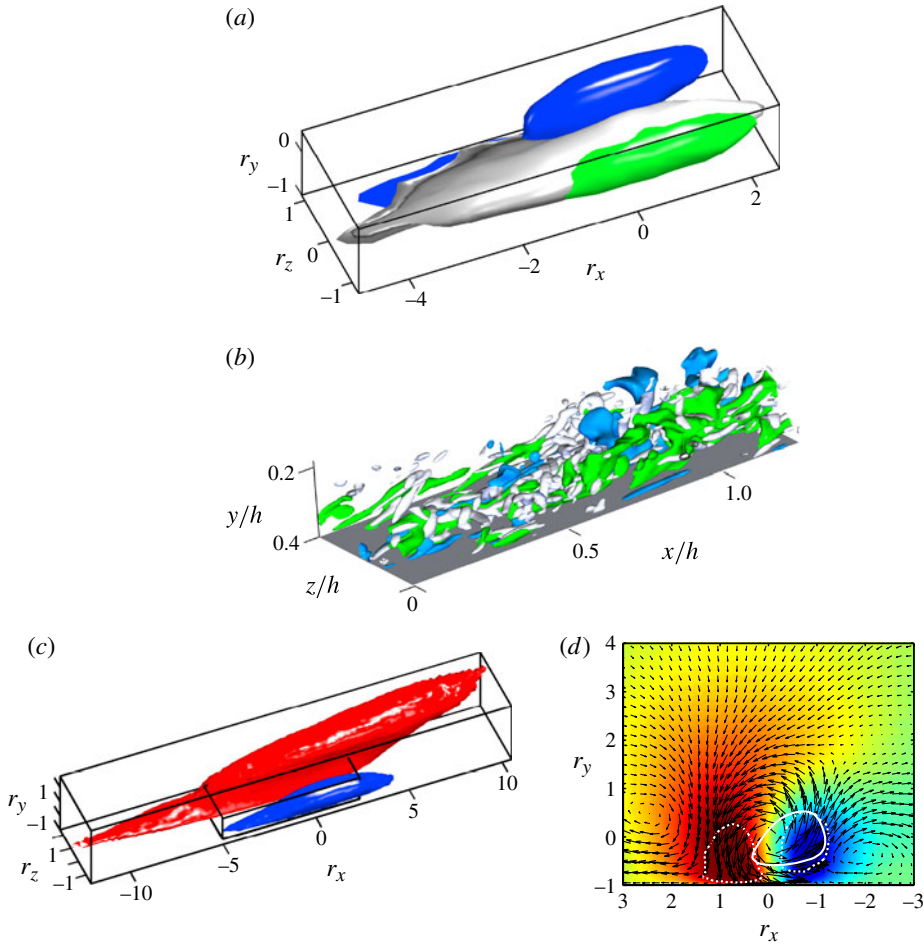
FIGURE 12. (Colour online) Flow fields conditioned to attached Q2–Q4 pairs in the logarithmic layer. L2000. (*a*) P.d.f.s of the points belonging to the Q2 (green), Q4 (blue) and clusters (grey). The isosurfaces plotted are 0.75 times the maximum value of the p.d.f.s for the Qs and 0.85 for the cluster. (*b*) Example of an instantaneous Q2–Q4 pair. Colour code as in (*a*). (Supplementary material is supplied alongside this article at http://dx.doi.org/10.1017/jfm.2011.524, the supplementary file is an interactive 3D object, click in the window to interact with it.) (*c*) Conditional streamwise perturbation velocity. The blue object is the low-speed isosurface, $u = -0.5u_\tau$. The red one is $+0.5u_\tau$. The heavy parallelepiped is a tight box around the conditional object in (*a*). The flow in (*a–c*) is from bottom-left to top-right. (*d*) Cross-section of the conditional field in (*c*) at $r_x = 0$. The arrows are the cross-flow (v, w), and the shaded map is the streamwise velocity ($u < 0$ in blue, $u > 0$ in red). The white dotted lines are 0.75 times the maximum value of the p.d.f. of the points belonging to the reference Q pair. The white solid line is 0.85 times the maximum value of the p.d.f. of the points belonging to the cluster.

6.1. *Sweep–ejection pairs*

Figure 12 shows the averaged flow field conditioned to the presence of a Q2–Q4 pair, which is defined whenever a Q2 has a neighbouring Q4 that satisfies the relative-height condition (4.3), and is within

$$|\delta_x| < 1.25 \quad \text{and} \quad |\delta_z| < 0.75. \tag{6.3}$$

Very similar results are obtained when the pair is defined as a Q4 with a neighbouring Q2. The conditional averages are then computed in the reference frame

$$r = 2(x - x^{(24)})/\Delta_y^{(24)}, \tag{6.4}$$

where $x^{(24)}$ is the midpoint of the line connecting the centres of the circumscribing boxes of the two Qs, and $\Delta_y^{(24)} = (\Delta_y^{(2)} + \Delta_y^{(4)})/2$ is the semi-sum of their vertical sizes. The axes are chosen so that $r_z > 0$ for the Q4.

Figure 12(*a*) shows the average shape of the pair and its associated cluster. As expected, the aspect ratios of this conditional object, approximately $4 \times 1 \times 1.5$ in the coordinate directions, are consistent with the p.d.f.s shown in figure 5, with two parallel Q^-s. The cluster is mostly lodged within the Q2, but it extends into the shear layer underneath the Q4. Note that the Q-pair is one-sided. No effort was made to prevent the formation of a conditional trio involving a second Q4 or Q2, but they did not appear in the statistics. Even so, and as we have already mentioned, the smooth conditional shape in this figure is not representative of the individual pairs of the flow, which are more complex. An example in the form of an interactive 3D object is supplied as supplementary material at http://dx.doi.org/10.1017/jfm.2011.524, click in the window to interact with it. It should be stressed again that while the averaged flow field in figure 12(*a*) is consistent with an asymmetric hairpin, the instantaneous pair is not.

Figure 12(*c*) shows the conditional streamwise velocity perturbation associated with the Q2–Q4 pairs. It has two streaks, elongated in the *x* direction, in qualitative agreement with the conical wakes reported by del Álamo *et al.* (2006) in the velocity fields conditioned to attached clusters. However, the figure shows that the two streaks are very different. For the isosurfaces used in the figure, the low-velocity object is only about as tall as the Q2, but the high-velocity perturbation is much larger, longer and taller than its associated Q4. The Q2 and its low-velocity streak seem to be engulfed within the larger high-velocity region. That is seen even more clearly in the cross-section in figure 12(*d*). As mentioned above, the velocity field obtained when the pair is defined with respect to the Q4, instead of the Q2, is very similar to that in figures 12(*c*) and 12(*d*), and does not differ too much from those obtained when conditioning on all Q2s or Q4s, confirming that most Q^-s are parts of pairs.

Similar findings were reported by Kim (1985) using the VITA technique in the buffer region, and by Ganapathisubramani (2008) for sinks of momentum, both at $y^+ \approx 100$ and at $y \approx 0.5h$. The low-velocity object lodged underneath the high-velocity overhang in figures 12(*c*) and 12(*d*) is clearly the same phenomenon as the low-velocity 'ramps' seen by many investigators in streamwise sections of the velocity field (e.g. Meinhart & Adrian 1995). Flores *et al.* (2007) noted that those ramps are actually long cylindrical tubes or cones, and figure 12(*c*) is most probably a conditional picture of a side wall of such a tube.

It was argued in del Álamo *et al.* (2006) that the clusters are too small to have created the low-velocity streak associated with them, and that they are probably a consequence of the streak, rather than a cause. That should probably now be rephrased as that they are a consequence of the Q2. Figures 12(*c*) and 12(*d*) suggest that even the low-speed streak is conditioned by the presence of a pre-existing larger sweep, which either creates it or, more probably, preferentially influences the location of the Q-pairs and clusters that serve to condition the figures.

6.2. *Large-scale organization*

The results presented up to now suggest that the building block of the Reynolds stresses is a pair of attached Q2s and Q4s, with a vortex cluster embedded within the Q2. The aspect ratios of those units are of the right order of magnitude for them to become comparable, when $\Delta_y \approx h$, to the large-scale motions defined by Adrian (2007). They are the best candidates that we have for the attached eddy hierarchy postulated by Townsend (1961).

On the other hand, they do not hint at a mechanism by which such structures, of size $O(h)$, can give rise to the very-long coherent structures ($\Delta_x \approx 20h$) in the central part of the channel, such as that in figure 8(*d*). Moreover, the procedure that we have used to identify them does not make use of the streamwise alignment detected in figure 11, suggesting that some undetected organization could exist at even larger scales. The only conditional structure detected up to now longer than a single Q is the high-velocity streak in figure 12(*c*).

It is tempting to explore the existence of 'supergroups' formed by Qs and clusters under somewhat laxer relational rules, but our attempts to extract physical meaning from such groups were not successful. It is very easy to form them by defining two objects as connected when they satisfy (6.3). Moreover, even if we enforce our usual rule that two objects can only be related if their heights differ by less than a factor of two, a supergroup can be formed with objects of many sizes, connected by intermediate chains of structures that differ little from their neighbours.

Such supergroups are longer and taller than individual Q^-s or clusters, and have statistical properties that can be interpreted as self-similar, although their aspect ratios, $8 \times 1 \times 2$, are only marginally more elongated than the single Q-pairs, and do not explain the longer global modes. In fact, although figure 11 proves the streamwise alignment of the pairs, the range of that ordering is not very long. Of the Q^-s in the logarithmic layer, roughly 55 % have another Q in front or behind, but only 13 % have both.

Moreover, most of the definite properties of the supergroups are retained when the positions of the Qs and clusters are randomized before they are allowed to connect, suggesting that the supergroups are little more than random juxtapositions of unrelated units, whose properties are determined by the volume fractions occupied by the different objects. They will not be discussed further in this paper.

It is interesting to mention at this point that recent visualization work suggests that the very-long structures mentioned above may be an exclusive feature of internal flows, and are not present in turbulent boundary layers (Hutchins *et al.* 2011; Dennis & Nickels 2011*b*; Lee & Sung 2011). Although generally using more limited statistics than those in the present paper, the three groups find that the longest structures in boundary layers have $\Delta_x \approx 6h$ and do not reach above $\Delta_y \approx 0.5h$. We have seen that the largest structures in channels extend well across the mid-plane, but Jiménez *et al.* (2010) already noted that boundary layers are shorter than channels and showed that many of the differences between the two flows are due to the effect of turbulent/irrotational intermittency in the corrugated edge of the boundary layer. That the wall-normal extent found in the papers just mentioned roughly coincides with the lower edge of the intermittent layer suggests that it may also be the interaction with irrotational fluid that limits the growth of the structures. The largest structures in boundary layers would not then be much longer than the self-similar attached eddies discussed in the previous sections and the problem with very-large-scale alignment would be exclusive to pipes and channels.

7. Conclusions

We have generalized to three dimensions the quadrant analysis of the intense Q events that contribute most to the tangential Reynolds stress in plane turbulent channels, with special emphasis on the logarithmic and outer layers. We have shown that they separate into wall-attached and wall-detached families.

The detached objects represent background fluctuations of the tangential Reynolds stress. They are isotropically oriented, and their contributions to the mean Reynolds stress cancel. Their dimensions and intensities are very similar to the strong fluctuations of the Reynolds stress in experimental flows with little mean momentum transport. Even in our turbulent channels, or in the atmospheric surface layer, the r.m.s. amplitude of the τ fluctuations is 2.5–3 times larger than their mean. Those detached Qs are small, with sizes that, at least at our Reynolds numbers, are of the order of a few Kolmogorov lengths.

The wall-attached Q^-s are larger, and carry most of the mean tangential Reynolds stress. At the identification threshold used in this paper, $H = 1.75$, they only fill 8 % of the volume of our channels, but they are responsible for roughly 60 % of the total Reynolds stresses at all wall distances. Most of the wall-attached events are sweeps or ejections, and form a self-similar family with aspect ratios $\Delta_x \approx 3\Delta_y$ and $\Delta_z \approx \Delta_y$, which agree well with the known dimensions of the *uv* cospectrum. There are very few attached 'countergradient' Q1s or Q3s.

When the Qs are extracted from one-dimensional sections of either our channels or experimental shear flows, their lengths appear to scale with the local Taylor microscale, but closer inspection reveals that they really span a wide range of scales, from the Kolmogorov to the integral length, and that the average length is not a representative quantity. In the channels, where objects can be classified in terms of their overall connected sizes, the thickness of objects in a given size class is more narrowly defined, suggesting that longer one-dimensional Qs also correspond statistically to larger three-dimensional objects in the experimental flows.

In fact, the similarities among the distributions of the one-dimensional Q surrogates in the very different shear flows in table 3 suggest that the fluctuations of the Reynolds stress are similar for all such flows at sufficiently high Reynolds numbers. In wall-bounded turbulence, the attached structures would simply be large fluctuations that reach the wall, because of their size, where they are modified by the inhomogeneity of the mean velocity profile.

The number of attached Q^-s decays away from the wall as Δ_y^{-2}. Since their wall-parallel area increases as Δ_y^2, the area covered by Q^-s of a given size is independent of Δ_y, and so is the fraction of the Reynolds stress carried by them. On the other hand, the volume fraction filled by the Q^-s increases with their size. Roughly 60 % of the total volume of the attached Q^-s is concentrated in a few very large Q2s that extend into the opposite half of the channel across the central plane. Those objects, with lengths of the order of 20h in our simulations, are probably the same as the very-large-scale structures discussed by several authors. They are visually composite objects, formed by the concatenation of smaller subunits, and do not form part of the self-similar family mentioned above.

The dimensions of the self-similar attached Q^-s are similar to those of the attached vortex clusters discussed by del Álamo *et al.* (2006). Most clusters are associated with at least one Q2, although the converse is not true. The number of attached clusters decays faster than the Qs, as Δ_y^{-3}, and the taller Qs do not have associated clusters.

The individual Q⁻s have fractal dimensions of the order of $D = 2$, slightly fuller than the clusters, whose dimension is $D \approx 1.7$. The thickness of their shells is 10–15 times the Kolmogorov length, at our Reynolds numbers, and they become more complicated as their sizes increase, suggesting that they might be described as 'sponges of flakes', in the same way that the vortex clusters might be described as 'sponges of strings'. Examples of both are given in figures 8 and 12.

Most of the Q2s and Q4s are grouped into side-by-side parallel pairs, mostly one-sided rather than symmetric trios. The predominant structure is formed by one such pair with a vortex cluster embedded within the base of the Q2 and underneath the Q4. As with the individual objects, the groups are self-similar, with aspect ratios $\Delta_x \approx 4\Delta_y$ and $\Delta_z \approx 1.5\Delta_y$. It is conjectured that those objects are the attached eddies of Townsend (1961), with which they share the dimensions and the stresses. The conditional velocity field around them shows that they are preferentially located in the side walls separating a low-velocity streak lodged underneath a larger high-velocity structure, which most probably coincides with the low-momentum ramps discussed by various authors.

The attached eddies tend to be aligned longitudinally with each other, but that organization does not extend far enough to explain the very long structures in the centre of the channel. Although roughly 55 % of the Q⁻s have another Q in front or behind, only 13 % have both. Attempts to identify larger super-groups that could explain the formation of the very-large-scale structures failed beyond what could be expected from purely random associations and did not reach the required aspect ratios, although some evidence is cited that this might only be a problem in internal turbulent flows.

Our simulations cover a factor of two in friction Reynolds numbers, in the range of many of the available experiments. The scalings that we have used in the figures are those that result in the best collapse of our simulations, and they are usually not ambiguous. Although it is dangerous to extrapolate beyond the range of the available data, that collapse suggests that our conclusions may apply to a wider range of Re_τ.

Acknowledgements

Supplementary movies are available at journals.cambridge.org/flm.

REFERENCES

ADRIAN, R. J. 2007 Hairpin vortex organization in wall turbulence. *Phys. Fluids* **19**, 041301.

ADRIAN, R. J., MEINHART, C. D. & TOMKINS, C. 2000 Vortex organization in the outer region of the turbulent boundary layer. *J. Fluid Mech.* **422**, 1–54.

DEL ÁLAMO, J. C., JIMÉNEZ, J., ZANDONADE, P. & MOSER, R. D. 2004 Scaling of the energy spectra of turbulent channels. *J. Fluid Mech.* **500**, 135–144.

DEL ÁLAMO, J. C., JIMÉNEZ, J., ZANDONADE, P. & MOSER, R. D. 2006 Self-similar vortex clusters in the turbulent logarithmic region. *J. Fluid Mech.* **561**, 329–358.

ANTONIA, R. A. & ATKINSON, J. D. 1973 High-order moments of Reynolds shear stress fluctuations in a turbulent boundary layer. *J. Fluid Mech.* **58**, 581–593.

ANTONIA, R. A., BISSET, D. & BROWNE, L. 1990 Effect of Reynolds number on the topology of the organized motion in a turbulent boundary layer. *J. Fluid Mech.* **213**, 267–286.

ANTONIA, R. A. & PEARSON, B. R. 1999 Low-order velocity structure functions in relatively high Reynolds number turbulence. *Europhys. Lett.* **48**, 163–169.

BALAKUMAR, B. J. & ADRIAN, R. J. 2007 Large- and very-large-scale motions in channel and boundary-layer flow. *Phil. Trans. R. Soc.* A **365**, 665–681.

BATCHELOR, G. K. 1953 *The Theory of Homogeneous Turbulence*. Cambridge University Press.

BERMEJO-MORENO, I. & PULLIN, D. I. 2008 On the non-local geometry of turbulence. *J. Fluid Mech.* **603**, 101–135.

BLACKBURN, H. M., MANSOUR, N. N. & CANTWELL, B. J. 1996 Topology of fine-scale motions in turbulent channel flow. *J. Fluid Mech.* **310**, 269–292.

BLACKWELDER, R. F. & KAPLAN, R. E. 1976 On the wall structure of the turbulent boundary layer. *J. Fluid Mech.* **76**, 89–112.

BOGARD, D. G. & TIEDERMAN, W. G. 1986 Burst detection with single-point velocity measurements. *J. Fluid Mech.* **162**, 389–413.

CORRSIN, S. 1958 Local isotropy in turbulent shear flow. Res. Memo 58B11, NACA.

DENNIS, D. J. C. & NICKELS, T. B. 2011a Experimental measurement of large-scale three-dimensional structures in a turbulent boundary layer. Part 1. Vortex packets. *J. Fluid Mech.* **673**, 180–217.

DENNIS, D. J. C. & NICKELS, T. B. 2011b Experimental measurement of large-scale three-dimensional structures in a turbulent boundary layer. Part 2. Long structures. *J. Fluid Mech.* **673**, 218–244.

FLORES, O. & JIMÉNEZ, J. 2008 The structure of momentum transfer in turbulent channels. In *Proceedings of Division Fluid Dynamics*, pp. PA–08. American Physical Society.

FLORES, O. & JIMÉNEZ, J. 2010a Hierarchy of minimal flow units in the logarithmic layer. *Phys. Fluids* **22**, 071704.

FLORES, O. & JIMÉNEZ, J. 2010b Log-layer dynamics in smooth and artificially rough turbulent channels. In *IUTAM Symposium Physics of Turbulence over Rough Walls* (ed. T. Nickels). pp. 93–98. Springer.

FLORES, O., JIMÉNEZ, J. & DEL ÁLAMO, J. C. 2007 Vorticity organization in the outer layer of turbulent channels with disturbed walls. *J. Fluid Mech.* **591**, 145–154.

GANAPATHISUBRAMANI, B. 2008 Statistical structure of momentum sources and sinks in the outer region of a turbulent boundary layer. *J. Fluid Mech.* **606**, 225–237.

GANAPATHISUBRAMANI, B., LONGMIRE, E. K. & MARUSIC, I. 2003 Characteristics of vortex packets in turbulent boundary layers. *J. Fluid Mech.* **478**, 33–46.

GUALA, M., HOMMEMA, S. E. & ADRIAN, R. J. 2006 Large-scale and very-large-scale motions in turbulent pipe flow. *J. Fluid Mech.* **554**, 521–542.

HOYAS, S. & JIMÉNEZ, J. 2006 Scaling of the velocity fluctuations in turbulent channels up to $Re_\tau = 2003$. *Phys. Fluids* **18**, 011702.

HUTCHINS, N. & MARUSIC, I. 2007a Evidence of very long meandering features in the logarithmic region of turbulent boundary layers. *J. Fluid Mech.* **579**, 467–477.

HUTCHINS, N. & MARUSIC, I. 2007b Large-scale influences in near-wall turbulence. *Phil. Trans. R. Soc.* A **365**, 647–664.

HUTCHINS, N., MONTY, J. P., GANAPATHISUBRAMANI, B., NG, H. C. H. & MARUSIC, I. 2011 Three-dimensional conditional structure of a high-Reynolds-number turbulent boundary layer. *J. Fluid Mech.* **673**, 255–285.

JIMÉNEZ, J. 1998 The largest scales of turbulence. In *CTR Annals of Research Briefs*, pp. 137–154. Stanford University.

JIMÉNEZ, J. 2012 Cascades in wall-bounded turbulence. *Annu. Rev. Fluid Mech.* **44**, 27–45.

JIMÉNEZ, J., DEL ÁLAMO, J. C. & FLORES, O. 2004 The large-scale dynamics of near-wall turbulence. *J. Fluid Mech.* **505**, 179–199.

JIMÉNEZ, J. & HOYAS, S. 2008 Turbulent fluctuations above the buffer layer of wall-bounded flows. *J. Fluid Mech.* **611**, 215–236.

JIMÉNEZ, J., HOYAS, S., SIMENS, M. P. & MIZUNO, Y. 2010 Turbulent boundary layers and channels at moderate Reynolds numbers. *J. Fluid Mech.* **657**, 335–360.

JIMÉNEZ, J. & MOIN, P. 1991 The minimal flow unit in near-wall turbulence. *J. Fluid Mech.* **225**, 213–240.

JIMÉNEZ, J., WRAY, A. A., SAFFMAN, P. G. & ROGALLO, R. S. 1993 The structure of intense vorticity in isotropic turbulence. *J. Fluid Mech.* **255**, 65–90.

KAILAS, S. V. & NARASIMHA, R. 1994 Similarity in vita-detected events in a nearly neutral atmospheric boundary layer. *Proc. R. Soc. Lond.* A **447**, 211–222.

KATUL, G., POGGI, D., CAVA, D. & FINNIGAN, J. 2006 The relative importance of ejections and sweeps to momentum transfer in the atmospheric boundary layer. *Boundary-Layer Meteorol.* **120** (3), 367–375.

KIM, H. T., KLINE, S. J. & REYNOLDS, W. C. 1971 The production of turbulence near a smooth wall in a turbulent boundary layer. *J. Fluid Mech.* **50**, 133–160.

KIM, J. 1985 Turbulence structures associated with the bursting event. *Phys. Fluids* **28**, 52–58.

KIM, J., MOIN, P. & MOSER, R. D. 1987 Turbulence statistics in fully developed channel flow at low Reynolds number. *J. Fluid Mech.* **177**, 133–166.

KIM, K. & ADRIAN, R. J. 1999 Very large-scale motion in the outer layer. *Phys. Fluids* **11** (2), 417–422.

KLINE, S. J., REYNOLDS, W. C., SCHRAUB, F. A. & RUNSTADLER, P. W. 1967 The structure of turbulent boundary layers. *J. Fluid Mech.* **30**, 741–773.

LEE, S.-H. & SUNG, H. J. 2011 Very-large-scale motions in a turbulent boundary layer. *J. Fluid Mech.* **673**, 80–120.

LOZANO-DURÁN, A. & JIMÉNEZ, J. 2010 Time-resolved evolution of the wall-bounded vorticity cascade. In *Proceedings of Division Fluid Dynamics*, pp. EB–3. American Physical Society.

LU, S. S. & WILLMARTH, W. W. 1973 Measurements of the structure of the Reynolds stress in a turbulent boundary layer. *J. Fluid Mech.* **60**, 481–511.

MEINHART, C. D. & ADRIAN, R. J. 1995 On the existence of uniform momentum zones in a turbulent boundary layer. *Phys. Fluids* **7**, 694–696.

MOISY, F. & JIMÉNEZ, J. 2004 Geometry and clustering of intense structures in isotropic turbulence. *J. Fluid Mech.* **513**, 111–133.

MOSER, R. D., KIM, J. & MANSOUR, N. N. 1999 Direct numerical simulation of turbulent channel flow up to $Re_\tau = 590$. *Phys. Fluids* **11**, 943–945.

NAGASOA, R. & HANDLER, R. A. 2003 Statistical analysis of coherent vortices near a free surface in a fully developed turbulence. *Phys. Fluids* **15** (2), 375–395.

NAKAGAWA, H. & NEZU, I. 1977 Prediction of the contributions to the Reynolds stress from bursting events in open-channel flows. *J. Fluid Mech.* **80**, 99–128.

NARASIMHA, R., KUMAR, S., PRABHU, A. & KAILAS, S. V. 2007 Turbulent flux events in a nearly neutral atmospheric boundary layer. *Phil. Trans. R. Soc.* A **365** (1852), 841–858.

PERRY, A. E., HENBEST, S. & CHONG, M. S. 1986 A theoretical and experimental study of wall turbulence. *J. Fluid Mech.* **165**, 163–199.

RAUPACH, M. R. 1981 Conditional statistics of Reynolds stress in rough-wall and smooth-wall turbulent boundary layers. *J. Fluid Mech.* **108**, 363–382.

ROBINSON, S. K. 1991 Coherent motions in the turbulent boundary layer. *Annu. Rev. Fluid Mech.* **23**, 601–639.

SADDOUGHI, S. G. & VEERAVALLI, S. V. 1994 Local isotropy in turbulent boundary-layers at high Reynolds number. *J. Fluid Mech.* **268**, 333–372.

SPALART, P. R. 1988 Direct simulation of a turbulent boundary layer up to $Re_\theta = 1410$. *J. Fluid Mech.* **187**, 61–98.

TANAHASHI, M., KANG, S., MIYAMOTO, T. & SHIOKAWA, S. 2004 Scaling law of fine scale eddies in turbulent channel flows up to $Re_\tau = 800$. *Intl J. Heat Fluid Flow* **25**, 331–341.

TOMKINS, C. & ADRIAN, R. J. 2003 Spanwise structure and scale growth in turbulent boundary layers. *J. Fluid Mech.* **490**, 37–74.

TOWNSEND, A. A. 1961 Equilibrium layers and wall turbulence. *J. Fluid Mech.* **11**, 97–120.

TOWNSEND, A. A. 1976 *The Structure of Turbulent Shear Flow*, 2nd edn. Cambridge University Press.

VAN ATTA, C. W. & WYNGAARD, J. C. 1975 On higher-order spectra of turbulence. *J. Fluid Mech.* **72**, 673–694.

WALLACE, J. M., ECKELMAN, H. & BRODKEY, R. S. 1972 The wall region in turbulent shear flow. *J. Fluid Mech.* **54**, 39–48.

WARK, C. E. & NAGIB, H. M. 1991 Experimental investigation of coherent structures in turbulent boundary layers. *J. Fluid Mech.* **230**, 183–208.

WILLMARTH, W. W. & LU, S. S. 1972 Structure of the Reynolds stress near the wall. *J. Fluid Mech.* **55**, 65–92.

ZHOU, J., ADRIAN, R. J., BALACHANDAR, S. & KENDALL, T. M. 1999 Mechanisms for generating coherent packets of hairpin vortices in channel flow. *J. Fluid Mech.* **387**, 353–396.